Hindawi
Complexity
Volume 2019, Article ID 3635621, 24 pages
https://doi.org/10.1155/2019/3635621

Research Article

Mechanical Response and Parametric Sensitivity Analyses of a Drainage Pipe under Multiphysical Coupling Conditions

Bin Li[1,2] **Hongyuan Fang**[1,2] **Kangjian Yang**[1,2] **Hang He**[1,2] **Peiling Tan**[1,2] **and Fuming Wang**[1,2]

[1]*College of Water Conservancy and Environmental Engineering, Zhengzhou University, No. 100, Science Road, Zhengzhou 450001, China*
[2]*Collaborative Innovation Center of Water Conservancy and Transportation Infrastructure Safety Protection, Henan Province, Zhengzhou University, Zhengzhou, Henan 450001, China*

Correspondence should be addressed to Hongyuan Fang; 18337192244@163.com

Received 20 June 2019; Revised 6 September 2019; Accepted 11 September 2019; Published 3 November 2019

Academic Editor: Oveis Abedinia

Current research was not dedicated to investigate the mechanical behavior of a concrete drainage pipe under multiphysical coupling conditions of overburden pressure, traffic loads, groundwater, and pipe fluids. This study proposes a new numerical solution method for coupled stress, seepage, and flow fields based on a validated finite element model. The model was developed by ABAQUS and FLUENT and then solved simultaneously using the MpCCI (mesh-based parallel-code coupling interface) platform. Results show that the tensile stress at the springline and the radial displacement at the crown (or invert) of the bell under the effect of groundwater alone were reduced by 50.5% and 38.1%, respectively, compared to the effect of traffic load alone. Parametric analyses show that vehicle speed and fluid height have a slight impact on the pipes. The soil cover depth, wheel pressure, and gasket strength are directly proportional to the pipe stress and vertical displacement. Within the scope of their respective changes, the pipe stresses were increased by 34.4%, 36.7%, and 28.5%, and the vertical displacements were increased by 124%, 95.85%, and 87.7%. The bedding and backfill strengths are proportional to the pipe stress and inversely proportional to the vertical displacement. Within the scope of their respective changes, the pipe stresses were increased by 18.2% and 20.0%, and the vertical displacements were decreased by 11.4% and 10.4%. Sensitivity analyses show that soil cover depth has a greatest impact on the pipe, followed by traffic load.

1. Introduction

Drainage pipes are an important component of urban underground infrastructure, and they play an important role in the daily operation of a city. According to the statistics of the National Bureau of Statistics of China, from 2004 to 2017, the total length of China's municipal drainage pipes increased from 219,000 kilometers to 630,000 kilometers (excluding drainage pipes installed in counties, towns, and villages), with a maximum annual growth rate of nearly 12% (Figure 1). Pipes are installed in complex geological and terrestrial environments and are subjected to coupled actions of various types of loading, often resulting in pipe damage and failure. Therefore, it is necessary to conduct in-depth studies on the mechanical behavior of a drainage pipe under coupled multiphysical conditions to prevent pipe damage and guide pipe maintenance.

Scholars have studied the mechanical behavior of pipes buried in dry and nondry soils as well as the fluid-structure interaction (FSI). Regarding pipes buried in dry soils, Fernando and Carter [1] studied the grounding shapes and material parameters of a tire using the Fourier analysis method, evaluated the tire's influence on the behavior of a pipe, and explored the maximum circumferential bending moment and axial thrust of the pipe cross section. Noor and Dhar [2] explored the effects of burial depth and pipe diameter on the mechanical properties of a pipe under traffic load (static load). García and Moore [3] studied the settlement and rotation of a

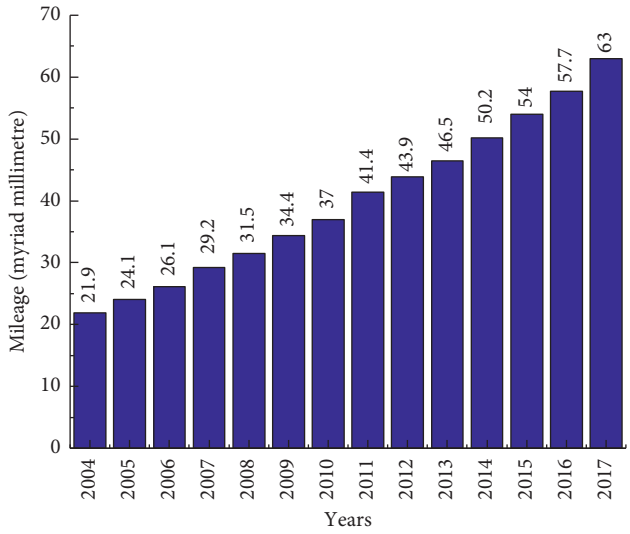

Figure 1: Development of municipal drainage pipes in China.

bell-and-spigot joint for a reinforced concrete pipe under different traffic loading locations and different pipe diameters through geotechnical tests and numerical simulations. Using full-scale physical tests, Lay and Brachman [4] investigated the structural response of a reinforced concrete pipe buried in dense, well-graded gravel soil considering different uniaxial design loads and soil cover depths (0.3, 0.6, and 0.9 m). Rakitin and Xu [5] studied the effects of soil cover depth, traffic load location, and magnitude on bending moment of a large reinforced concrete pipe with a diameter of 1400 mm by the geotechnical centrifuge test. Using the FE method, Meesawasd et al. [6] explored the effects of burial depth, traffic load, vehicle speed, and vehicle type on pipe stress distribution. By using a 3D FE model, Alzabeebee et al. [7] verified the design methods adopted for current British pipes and discussed the relationship between the pipe diameter and maximum vertical displacement. The results demonstrated that the influence of traffic load on the maximum axial force of a pipe is greatly affected by the burial depth; when the burial depth exceeds 3 m, the influence of a traffic load is negligible. Rakitin and Xu [8] conducted geotechnical centrifuge tests on a large-diameter reinforced concrete pipe with gasketed bell-and-spigot joints and studied the vertical displacement of the pipe as well as the rotation of the joints under various traffic load combinations. By numerically modeling geotechnical centrifuge tests, Xu et al. [9] studied the mechanical responses (under static loading) of a large-diameter concrete pipe with bell-and-spigot joints under different loads, soil stiffness values, and loading locations.

The prediction and control of subgrade settlements are key factors affecting the quality of infrastructures construction [10]. Wang et al. [11] investigated and discussed the soil behavior under multiphysical coupling conditions in detail. Zhang and Shao [12] used the Galerkin discrete and Newmark-β methods to observe the dynamic response of a pipe buried in saturated soil subjected to traffic loads and evaluated the effects of the permeability coefficient, flow velocity, Poisson's ratio, and void ratio on the dynamic pipe response. Using the 2D FE method, Randeniya et al. [13] studied the mechanical response of a pipe buried in semidry soil subjected to traffic load. Their results showed that the mechanical response of a pipe buried in partially saturated soil under traffic load was quite different from that of a pipe buried in dry soil. Al-Khazaali et al. [14] investigated the numerical analysis of buried rigid and flexible pipes by extending the effective stress analysis and the modified effective stress analysis approaches for saturated and unsaturated soils. The results of pipe displacement, strain, and internal force show that soil trenching in unsaturated soil contributes to finite deformation near the buried pipe and leads to lower internal force. Robert and Thusyanthan [15] conducted full-scale tests and finite element parametric studies on pipes buried in unsaturated soil and studied the effects of soil water content, soil cover height, and soil relative density on the uplift peak value of pipes. Williams et al. [16] studied the plane strain uplift resistance of pipes in saturated sand to reveal the effects of low relative density backfill and partially drained soil response on the uplift resistance of pipes, and the results suggested that the soil state has a strong influence on the pipe-soil failure mechanism.

Regarding fluid-structure interaction problems between the pipes and fluid filled in pipes, Tijsseling [17] described in detail the concept of pipe structure-fluid coupling and concluded that the structural response of a pipe interacts with the pipe fluid and vibration of the pipe inevitably affects the dynamic fluid pressure. Wiggert and Tijsseling [18] summarized the mechanical behavior that induces pipe-fluid coupling issues and proposed methods for modeling fluid-solid coupled scenarios. Based on the FE method, Belostosky et al. [19] discussed the structure-fluid interaction issues for the pipe structure-fluid coupling scenarios. Ferràs et al. [20] used a 4-equation model to study the fluid-structure interaction in a straight pipe friction coupling mechanism. The main focus lies on the friction coupling modeling considering skin and dry friction. Using the 3D FE method, Li et al. [21] extensively studied the mechanical response of a corroded pipe under coupling actions of overburden pressure, traffic load, and pipe fluid. Dagli and Ergut [22] used Rayleigh theory to study the dynamic characteristics of fluid conveying pipes and the influence of nonclassical boundary conditions on the natural frequency of pipes, in which Euler equation was used to simulate the flow behavior in pipes.

The above studies mainly focused on the effects of parameters related to soil, pipes, and traffic loads on the pipe's mechanical response or only considered the effects of seepage or flow field on a pipe. Based on the previous studies, this paper utilized the advanced FE model, numerical solution tools, and full-scale test to fully consider the coupled effects of stress field generated by overburden pressure and traffic load, FSI induced by fluid flow, and seepage field due to groundwater on concrete drainage pipe, and a parametric analysis was conducted for each parameter affecting the mechanical properties of the pipe. Based on the research results, a new numerical solution method validated by a full-scale test was proposed to solve the coupled stress-seepage-flow fields of a buried pipe. The main objectives of this study were to (1) compare the mechanical response of a drainage

pipe under single physical and coupled multiphysical fields; (2) carry out parametric analyses for scenarios of coupled multiphysical fields using the variable controlling method to explore the influences of individual parameters on the mechanical behavior of the pipe; (3) use the normalization method to conduct sensitivity analyses of the parameters affecting the mechanisms of the pipe to identify the factors that have the greatest impact on the pipe; and (4) provide insight into numerical solutions for the mechanical properties of the buried pipe under the action of coupled multiphysical fields.

2. Full-Scale Test Configuration

The constructed 3D FE model was verified utilizing a full-scale test, which was developed as a part of the new numerical solution method proposed for coupled stress, seepage, and flow fields. A series of full-scale tests were conducted to investigate the performance of concrete drainage pipes with 1000 mm diameter and 100 mm thickness. However, because the buried depth of the groundwater level in the test site is far greater than that of the pipe, groundwater was not considered in the full-scale test, i.e., the field test was carried out under the coupled conditions of overburden pressure, vehicle load, and pipe fluid. The strain gauges were instrumented on the pipes to observe their behavior during the applications of the coupled loads. Figure 2 demonstrates the instrumentation of the concrete pipes used in the field test. The pipes were installed and instrumented by excavating a test pit of 2700 mm depth (soil cover depth was 1000 mm).

Vehicle load was applied by a single-axle two-wheeled heavy truck equipped with rated blocks and moving at various speeds. The parameters of the axle and simplified tire tread imprint (a rectangle of 0.2 m × 0.6 m) measured in the test are displayed in Figure 3. The mass of the truck and rated blocks were 13 t and 1.0 t, respectively. The vehicle loads applied to the field test were adjusted by loading and unloading the standard blocks. Assuming that the front and rear wheels account for 1/3 and 2/3 of the total vehicle weight, respectively, the wheel pressure can be calculated by

$$P = \frac{2F/3}{4A} = \frac{F}{6A}, \tag{1}$$

where P is the pressure of each tire applied to the ground, F is the total weight of the truck and rated blocks, and A is the area of each tire.

Fluid load was applied by brick inspection wells built on both sides of the test pipes. The inspection wells filled with water were connected using a fire hose, and the water in the pipes and the inspection wells circulated by means of several water pumps, thus generating fluid load. The height of the fluid in the pipe, i.e., the flow rate, is increased by increasing the water pump, as shown in Figure 4.

3. Description of the FE Model

3.1. Structure Model. The pipe-soil system model was created in ABAQUS, and the dimensions are 8 m × 8 m × 12 m. The bedding was made of 90° arc-shaped gravel that has a thickness of 0.5 m. The pipe is backfilled and compacted within 0.5 m on both sides and top of the pipe, as shown in Figure 5. The pipe model consists of six pipe segments and five gasketed bell-and-spigot joints. The geometrical parameters of each pipe segment were selected according to *Concrete and Reinforced Concrete Sewer Pipes* (GB/T 11836-2009) [23] (Figure 6(a)). For modeling simplicity and fast convergence, the bell-and-spigot joint model was simplified, as shown in Figure 6(b).

Gaskets are typically made of soft materials (e.g., rubber) with a low modulus of elasticity [24] to ensure sealing of the bell-and-spigot joints. During pipe installation, a gasket is compressed, resulting in an expansion force. Consequently, outward and inward circumferential pressures are created on the bell and spigot, respectively. In order to simulate this behavior, this paper simplified the cross section of a gasket into a rectangle with a width of 24 mm and a height of 11.5 mm (Figure 7) [9, 25]. Before numerical simulation, the soil structure was first "killed". A circumferential pressure was then applied to the outer surface of the gasket to make the gasket's circumferential compressive stress reach approximately 0.3 MPa [9]. Next, the soil structure was "activated" and the circumferential pressure was released to free the gasket. Under the action of the gasket expansion force, the bell and the spigot were pressed outward and inward, respectively. The above procedure simulates the extrusion and sealing actions of the gasket applied to the bell-and-spigot joint during the pipe assembly process.

Mesh quality is an important factor to determine the accuracy of dynamic calculation. To minimize the distortion wave effect in dynamic analyses, the size of the mesh must be less than the maximum value, which is one-tenth of the wavelength λ [26], as presented in equation (2):

$$f = \frac{C_s}{10 \cdot \Delta l} = \frac{\omega}{2\pi}, \tag{2}$$

where C_s = shear-wave velocity (m/s), Δl = maximum mesh element size (m), f = frequency of excitation (Hz), and ω = circular frequency of excitation (rad/s).

Considering the complexity of the model, the model meshes were divided by Hypermesh 13.0 software. The minimum mesh numbers of soil, pipe, gasket, and fluid satisfying the calculation accuracy were discretized by 44,400, 33,522, 1,200, and 19,500 volumetric elements according to equation (2), respectively, and the element type was 3D solid eight-node reduction integral element (C3D8R) with controlled hourglass. The generated mesh is presented in Figure 8.

In order to further analyze the influence of mesh size on the numerical results, the sensitivity analyses of the mesh size of the model components under three different mesh discretization schemes were carried out by comparing the maximum pipe stress (σ_{max}) with the results observed from the test pipes, and the calculation time (T) was another comparison item. The maximum pipe stress and calculation time under three different mesh discretization schemes are shown in Table 1. It can be seen that the difference between the pipe stress in scheme 1 and the test results is 5.13% and

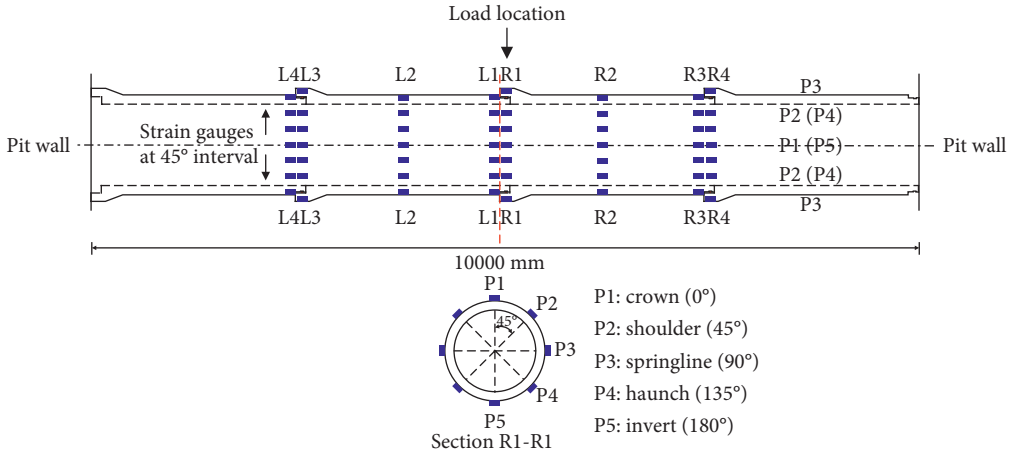

Figure 2: Instrumentation on field pipe sections.

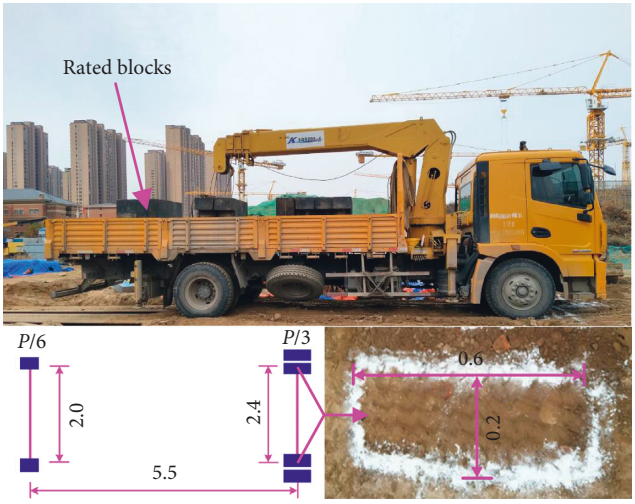

Figure 3: Application of traffic load.

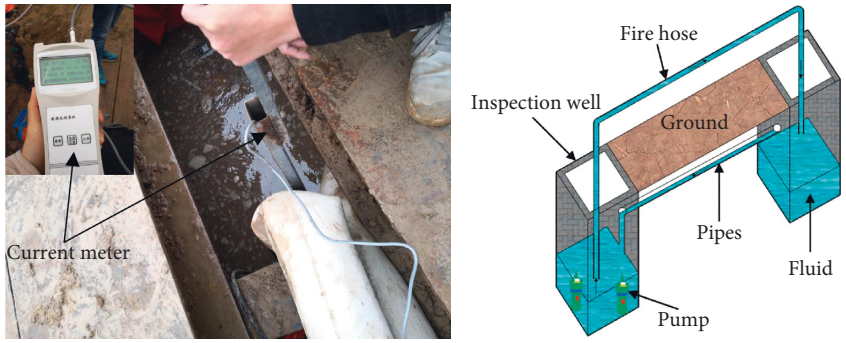

Figure 4: Application of fluid load.

that of scheme 2 and scheme 3 is more than 7.5% and 10.3%. Additionally, compared with schemes 2 and 3, scheme 1 can save calculation time by 26.7% and 45.0%. Therefore, the mesh size determined according to equation (2) can not only meet the calculation accuracy but also ensure the calculation efficiency.

3.2. Fluid Model. In the fluid model, a two-phase flow consisting of air and fluid was considered inside the pipe. It was assumed that the fluid occupied the lower half of the pipe, and the remaining half was filled with air. The pipe fluid model was created using FLUENT, and the mesh was created using ICEM CFD.

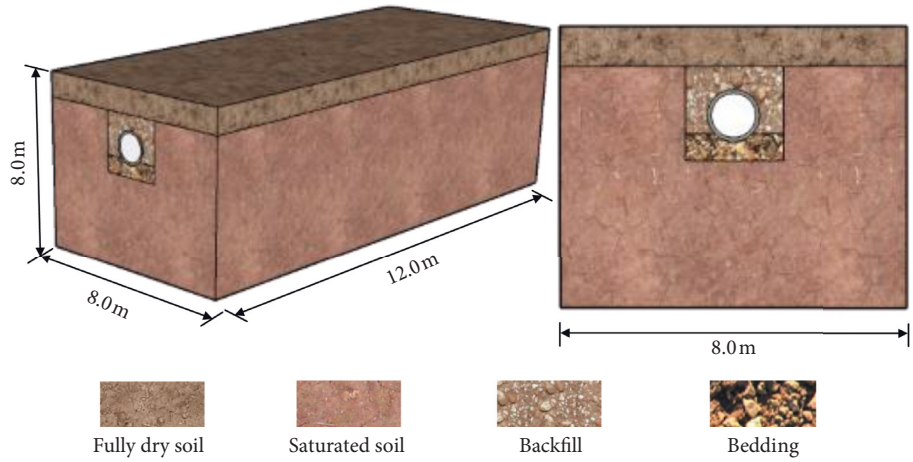

Figure 5: Computational model (groundwater level is 1.0 m below the springline).

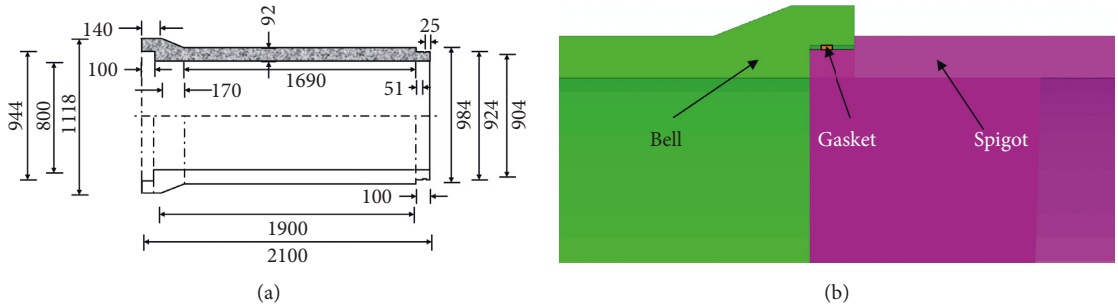

Figure 6: Details of (a) pipe segment and (b) gasketed bell-and-spigot joint.

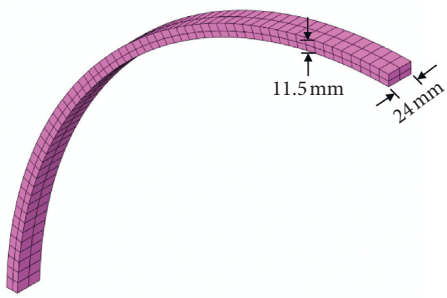

Figure 7: Gasket mesh and geometry.

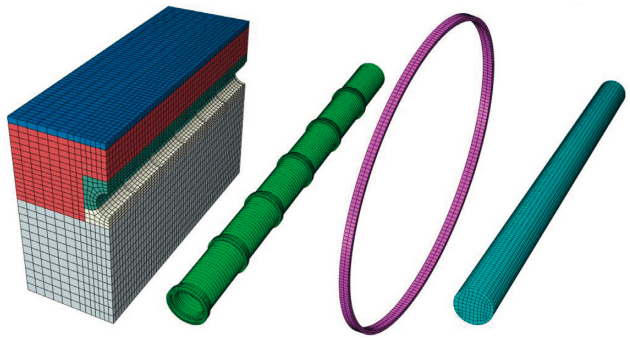

Figure 8: Mesh discretization of the FE model (not to scale).

3.2.1. Fluid-Air Model. There are three multiphase flow models in FLUENT: Volume of fluid model (VOF) [27], Mixture model [28], and Eulerian model [29]. The Mixture model is a simplified multiphase flow model for simulating multiphase flows with different velocities in each phase. The Eulerian model is used primarily to simulate the interaction of particle groups with fluids. The VOF model is a surface-tracking method applied to fixed Eulerian mesh, which can be used to study the interface position between several immiscible fluids. By solving a single momentum equation and tracking the volume fraction of each fluid in the calculation domain, two or more immiscible fluids can be simulated to effectively solve the two-phase flow problem.

In order to investigate which multiphase flow model is more suitable for characterizing the fluid-air model in this study, the maximum pipe stresses under the VOF model, Mixture model, and Eulerian model and the results collected from the strain gauges were compared, and the comparison items also include the calculation time, as shown in Table 2. It can be seen that the differences between the pipe stresses in the VOF model, Mixture model, and Eulerian model and the test results are very close, being 5.13%, 5.22%, and 5.27%, respectively, indicating that these models all meet the requirements in terms of calculation accuracy. Considering the computational efficiency, the VOF model can save 14.8% and 32.4% computational time compared with the Mixture model and Eulerian model. Therefore, only the VOF model

Table 1: Sensitivity analysis of the model mesh size.

Scheme	Scheme 1				Scheme 2				Scheme 3			
Component	Soil	Pipe	Gasket	Fluid	Soil	Pipe	Gasket	Fluid	Soil	Pipe	Gasket	Fluid
Number (10^4)	4.44	3.35	0.12	1.95	4.76	3.52	0.13	2.12	5.02	3.72	0.14	2.33
Test-σ_{max} (MPa)	1.48											
FE-σ_{max} (MPa)	1.56				1.60				1.65			
T (h)	5.5				7.5				10			

Note. Scheme 1 was conducted according to equation (2). The FE-σ_{max} and t were obtained based on the basic parameters mentioned in Section 5.3, without considering groundwater.

Table 2: Sensitivity analysis of fluid-air models.

Model	VOF	Mixture	Eulerian
Test-σ_{max} (MPa)	1.48000		
FE-σ_{max} (MPa)	1.56000	1.56156	1.56234
T (h)	5.50	8.13	6.46

Note. The FE-σ_{max} and t were obtained based on the basic parameters mentioned in Section 5.3, without considering groundwater.

Table 3: Sensitivity analysis of turbulent models.

Model	RNG k-ε	SST k-ω
Test-σ_{max} (MPa)	1.48000	
FE-σ_{max} (MPa)	1.56000	1.56148
T (h)	5.5	8.8

Note. The FE-σ_{max} and t were obtained based on the basic parameters mentioned in Section 5.3, without considering groundwater.

meets the requirements in terms of calculation accuracy and efficiency.

3.2.2. Turbulence Model. In general, the fluid inside the pipe is in multiple turbulent states. The common turbulence models used in FLUENT include the standard k-ε [30] model, RNG k-ε model [31], standard k-ω model [32], and SST k-ω model [27]. The standard k-ε model is a semi-empirical formula, which is only suitable for the completely turbulent flow process. The RNG k-ε model includes a modification to the standard k-ε model. This modification includes an additional parameter, R_ε, which obviously improves the accuracy of rapidly strained flows. In addition, it also provides an analytical formula for turbulent Prandtl numbers α_k and α_ε, while the standard k-ε model uses constant values. The standard k-ω model is based on the Wilcox k-ω model, which is modified to consider low Reynolds number, compressibility, and shear flow propagation. The SST k-ω model was developed by Menter, which is independent of the k-ω model in a wide range of fields, making the SST k-ω model more accurate and reliable than the standard k-ω model.

Analysis shows that the RNG k-ε model and the SST k-ω model have a higher calculation accuracy and wide application range than the standard k-ε model and the standard k-ω model. Therefore, only the maximum pipe stresses under the RNG k-ε model and the SST k-ω model were compared with the test results, and the calculation time was also included in the comparison, as shown in Table 3. Table 3 shows that the differences between the maximum pipe stresses of the RNG k-ε model and the SST k-ω model and the field results are 5.13% and 5.22%, respectively, demonstrating that the RNG k-ε model and the SST k-ω model can well predict the pipe stress. In addition, the RNG k-ε model saves 14.8% of the calculation time compared with the SST k-ω model. Therefore, the RNG k-ε model was chosen to simulate the turbulent characteristics of the fluid in the pipes.

In the RNG k-ε model, small-scale effects were reflected through large-scale motions and in modified viscosity terms, so that these small-scale motions could be systematically removed from the governing equations. The resulting k-equation and ε equation are as follows:

$$\frac{\partial(\rho k)}{\partial t}+\frac{\partial(\rho k u_i)}{\partial x_i}=\frac{\partial}{\partial x_j}\left(a_k u_{\text{eff}}\frac{\partial k}{\partial x_j}\right)+G_{k+}\rho\varepsilon,$$

$$\frac{\partial(\rho\varepsilon)}{\partial t}+\frac{\partial(\rho\varepsilon u_i)}{\partial x_i}=\frac{\partial}{\partial x_j}\left(a_\varepsilon u_{\text{eff}}\frac{\partial \varepsilon}{\partial x_j}\right)+\frac{C_{1\varepsilon}^{*}\varepsilon}{K}G_{k-}C_{2\varepsilon}\rho\frac{\varepsilon^2}{k}, \tag{3}$$

where $C_u = 0.0845$, $C_{\varepsilon 1}^{*} = C_{\varepsilon 1} - (\eta(1-(\eta/\eta_0)))/(1+\beta\eta^3)$, $C_{\varepsilon 1} = 1.42$, $C_{\varepsilon 2} = 1.68$, $\eta = (2E_{ij}\cdot E_{ij})^{0.5}(k/\varepsilon)$, $\eta_0 = 4.377$, $\beta = 0.012$, and $E_{ij} = 1/2((\partial u_i/\partial x_j)+(\partial u_j/\partial x_i))$.

3.3. Traffic Load. In this study, traffic load was assumed to be applied directly above the pipe and moving at a certain speed. With a wheelbase of 2.4 m, the traffic load was symmetrically distributed on both sides of the pipe axis. The tire grounding area is a rectangle of 0.2 m × 0.6 m. The load was applied using the "VDLOAD" subroutine written in Fortran. The Fortran compilation flowchart is shown in Figure 9. The traffic load function used the sinusoidal expression shown in equation (4) [33]. This function considers the dependency of traffic loading on the static wheel load, the traffic speed, and the road condition (roughness):

$$F_t = F + F_0 \sin \omega t, \tag{4}$$

where $F_0 = G_0\mu_{\omega/r}(y)\omega^2$, $\omega = 2\pi\nu/l$, F = the static vehicle wheel load, G_0 = unsprung weight, whose value was taken as 280 Ns^2/m, $\mu_{\omega/r}(y)$ = road roughness function, with a value of 2.5 mm, ν = vehicle speed, l = geometric curve wavelength of the pavement, whose value was considered to be equal to 6.5 m, and t is the duration time of the traffic load.

Taking $F = 100$ kN as an example, the amplitudes and frequencies of the traffic load at different vehicle speeds (30 km/h, 45 km/h, 60 km/h, 75 km/h, and 90 km/h) are shown in Table 4. The time-history curves in one cycle are shown in Figure 10.

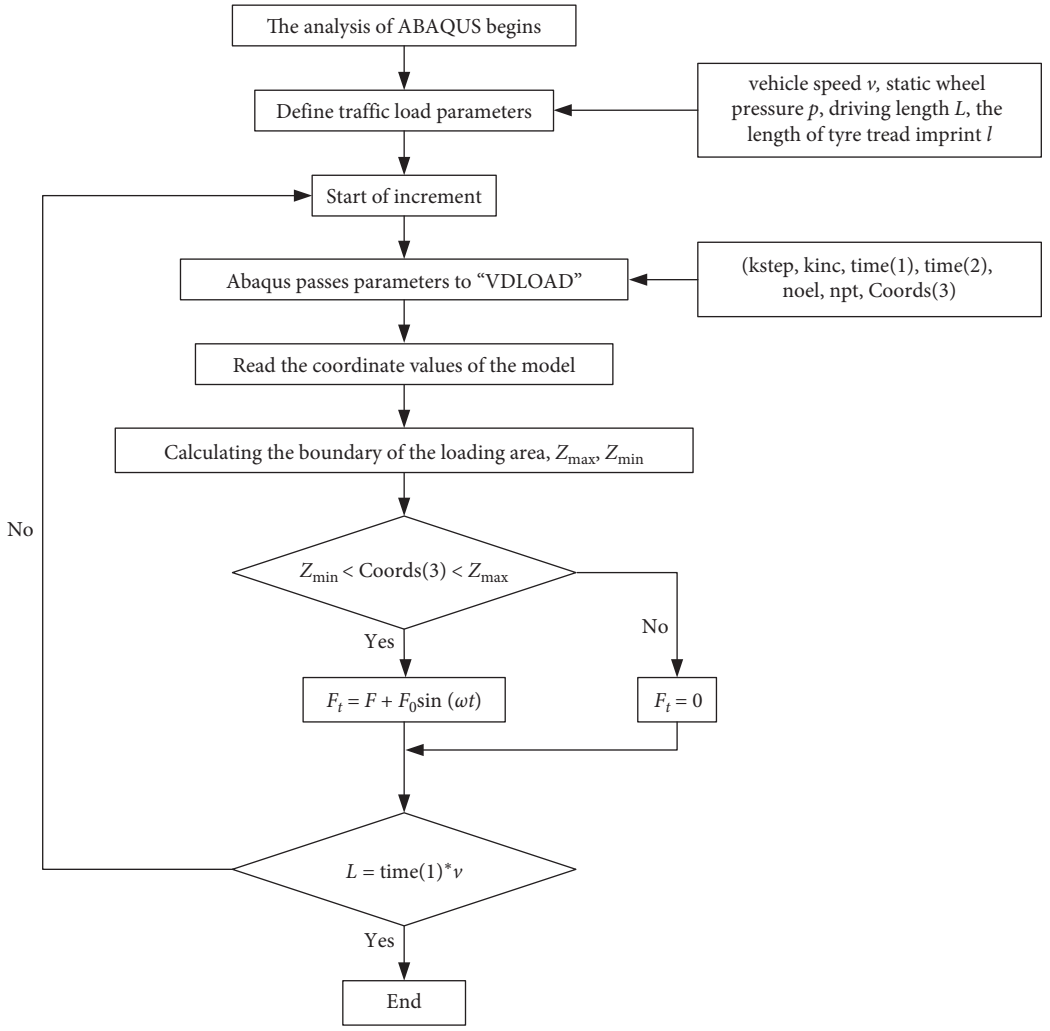

Figure 9: Flowchart for compiling the traffic load subroutine.

Table 4: Parameters of the traffic load.

v (km/h)	F (kN)	ω (rad/s)	F_0 (kN)
30	100	8.73	0.05
45	100	13.09	0.12
60	100	17.45	0.21
75	100	21.82	0.33
90	100	26.18	0.48

3.4. Materials. The Mohr–Coulomb constitutive model was applied to the soil. The pipe was described by the C30 typical Concrete Damaged Plasticity (CDP) constitutive model proposed by Lee and Fenves [34], which provides a universal material model for the mechanical response of concrete structures under dynamic loading. The gasket is composed of a superelastic material that exhibits nonlinearity under compression. The effect of a gasket on the bell-and-spigot joint depends on the degree of compression [35]. Studies by García and Moore [36] and Xu et al. [9] have shown that effect of a gasket on a bell-and-spigot joint is not much

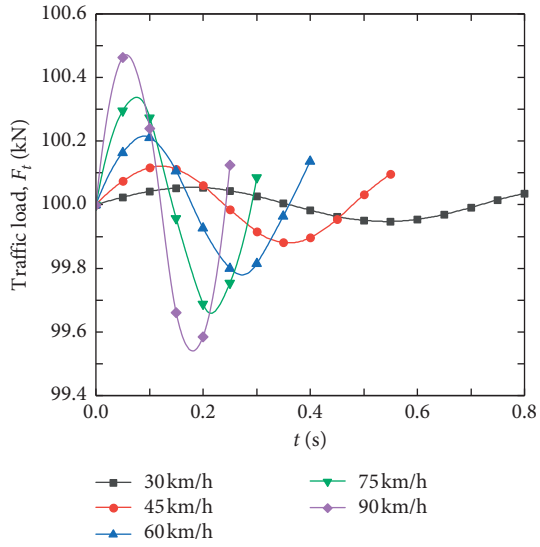

Figure 10: Traffic load time-history curve in a cycle.

different, even if the gasket is treated as an elastic material or a superelastic material. Therefore, for low computational cost, it is necessary and reasonable to assume the gasket as an elastic material. The physical and mechanical properties of the material of the basic case are shown in Table 5.

3.5. Contact and Boundary Conditions. Sliding and separating were modeled at the pipe-soil interface, the contact interfaces between the gasket outer surface and bell, and between the gasket inner surface and spigot. In the tangential direction of the contact surface, the stiffness (penalty) method that permits some relative motion of the surfaces (i.e., "elastic slip") when they should be sticking was used. While the surfaces are sticking (i.e., $\overline{\tau} < \overline{\tau}_{\text{crit}}$), the magnitude of sliding is limited to elastic slip. Analyses where μ (soil-pipe interface friction coefficient) was varied between 0.2 and 0.4 suggested that the effects of those changes in μ on the behavior of the pipe are negligible [37]. Therefore, all analyses feature a μ value of 0.3. In the normal direction of the contact surface, the classical Lagrange multiplier method of constraint enforcement was used.

The boundary conditions involved in the model in this study mainly include pipe-soil system displacement and pore pressure, fluid inlet and outlet, and pipe wall-fluid. The above boundary conditions were set as follows:

(1) Displacement boundary conditions of the pipe-soil system: during the compression phase of a gasket, the soil structure was "killed." At this time, only the displacement freedom in the three directions at the two ends of the pipe segment was restrained. During applications of gravity and traffic loads, the soil structure was "activated." At this time, an infinite element transmission boundary utilizing the $1/r$ far-field attenuation shape function was adopted to reduce the influence of the stress wave reflection at the force-displacement boundary [38]. The construction mode of the infinite element is shown in Figure 11. The shape functions of 1, 2, 3, 4 and 5, 6, 7, 8 nodes were selected as

$$\begin{aligned} N_i' &= 0.25\left(1+\eta\eta_i\right)\left(1+\zeta\zeta_i\right)f_1, \quad i = 1,2,3,4, \\ N_i' &= 0.25\left(1+\eta\eta_i\right)\left(1+\zeta\zeta_i\right)f_2, \quad i = 5,6,7,8, \end{aligned} \tag{5}$$

where f_1 and f_2 are the attenuation functions, expressed as

$$\begin{aligned} f_1 &= \frac{-2\xi}{1-\xi}, \\ f_2 &= \frac{1+\xi}{1-\xi}. \end{aligned} \tag{6}$$

For any point in an infinite element,

$$r = \sum_{i=1}^{4} N_i' r_1 + \sum_{i=5}^{8} N_i' r_2, \tag{7}$$

ξ can be given *as*

Table 5: Physical and mechanical properties of materials of the basic case.

Parameter	Unit	Value
Subgrade (dry)		
Density, ρ	kg·m^{-3}	1850
Elastic modulus, E	MPa	15.0
Poisson's ration, $\boldsymbol{v}$	—	0.25
Friction angle, φ	°	20.0
Damping, α	—	0.32
Subgrade (saturated)		
Density, ρ_{d}	kg·m^{-3}	1400
Elastic modulus, E	MPa	15.0
Poisson's ration, $\boldsymbol{v}$	—	0.3
Friction angle, φ	°	15.0
Damping, α	—	0.32
Permeability coefficient, k	m/s	$1e-07$
Void ratio, e	—	1.2
Backfill		
Density, ρ	kg·m^{-3}	2000
Elastic modulus, E	MPa	20.0
Poisson's ration, $\boldsymbol{v}$	—	0.25
Friction angle, φ	°	20.0
Damping, α	—	0.34
Void ratio, e	—	0.5
Permeability coefficient, k	m/s	$1e-08$
Bedding		
Density, ρ	kg·m^{-3}	2400
Elastic modulus, E	MPa	200.0
Poisson's ration, $\boldsymbol{v}$	—	0.2
Friction angle, φ	°	30.0
Damping, α	—	0.20
Void ratio, e	—	0.6
Permeability coefficient, k	m/s	$1e-06$
Gasket		
Elastic modulus, E	MPa	4.00
Poisson's ration, $\boldsymbol{v}$	—	0.40
Concrete		
Elastic modulus, E	MPa	30000
Poisson's ratio, $\boldsymbol{v}$	—	0.20
Density, ρ	kg·m^{-3}	2400
Permeability coefficient, k	m/s	$1e-12$
Void ratio, e	—	0.01
Dilation angle, ψ	°	30.0
Flow potential eccentricity, e	—	0.10
Viscosity parameter, μ	—	0.005

$$\xi = 1 - \frac{2\left(r_1 - r_2\right)}{r - r_2 + 2\left(r_1 - r_2\right)}. \tag{8}$$

It can be verified by equation (8) that when ξ is taken as -1, 0, and 1, r is equal to r_1, r_2, and ∞. Equation (8) can be expressed as

$$\xi = 1 - \frac{2(\alpha - 1)}{r + 2(\alpha - 2)r_2}. \tag{9}$$

Equation (9) shows that ξ exhibits $1/r$ attenuation, and the purpose of adjusting the node in progress can be achieved by changing the value of α.

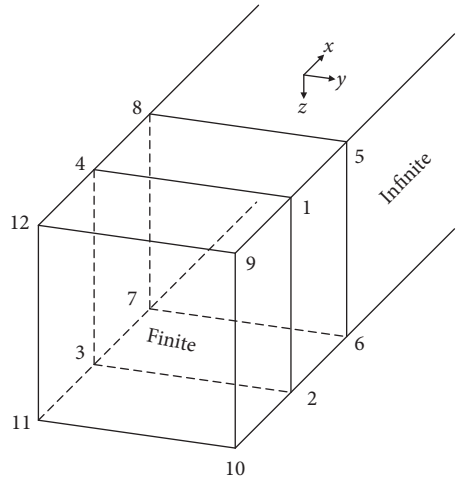

Figure 11: Infinite element node location.

(2) Pore pressure boundary condition of the pipe-soil system: pore water pressure was set to $\rho_w g \times (Y - y)$ at the YZ boundary surface of the soil body, where ρ_w is the mass density of water, g is the gravitational acceleration, Y is the coordinate value of the groundwater level, and y is the coordinate value of any point below the groundwater level. Pore pressure was set to zero (por = 0) at the groundwater level (Figure 12(a)).

(3) Fluid boundary condition (Figure 12(b)):

(i) Inlet: fluid entered the pipe at a rate of 1.0 m/s, and the flow rate was calculated based on the flow and the pipe inlet cross section.

(ii) Outlet: zero pressure was assumed at the pipe outlet (i.e., the pipe outlet was connected to the atmosphere).

(4) Pipe wall-fluid boundary condition: the standard wall function was employed to simulate the flow-pipe inner wall. Near-wall flow conditions were assumed for the pipe flow simulation [39], as shown in equation (10):

$$U^* = \frac{1}{k}\ln(Ey^*), \quad y^* > 11.2,$$
$$U^* = y^*, \quad y^* \le 11.2, \tag{10}$$

where $U^* \equiv (U_P C_\mu^{(1/4)} k_P^{(1/2)})/(\tau_w/\rho)$, $y^* \equiv (\rho C_\mu^{1/4} k_P^{1/2} y_P)/(\mu^*)$, $k = 0.42$, and $E = 8.955$. U_p is the average flow rate of the fluid at point P, k_p is the turbulent kinetic energy at point P, y_p is the distance from point P to the wall, and $\mu^* = 0{\cdot}00089$ kg/(m/s) is the dynamic viscosity coefficient of the fluid.

3.6. ABAQUS and FLUENT Coupled Solution Method. The FSI was achieved by using the professional interface software MpCCI to solve ABAQUS (structure) and FLUENT (fluid) simultaneously. MpCCI is a mesh-based parallel code coupling interface developed by the Fraunhofer Institute in Germany. It can solve large-scale and complex engineering problems by adopting computer parallel technology. Even without the capability to simulate coupled multiphysical conditions, MpCCI can provide interfaces for various types of finite element software to model multiphysical coupling [40, 41].

The difference in precision requirements and discrete methods between the structure and fluid meshes leads to a general nonmatching between the meshes in the structure and fluid subdomains. Therefore, a precise interpolation method is needed in FSI interaction simulations. The data exchange procedure used in this study can be divided into two main steps:

Step 1 (association). Neighborhood search was carried out on each point in the target mesh to find the nearest element in the source mesh to form a node-element relationship for subsequent data interpolation.

Step 2 (interpolation). Two quantities need to be exchanged at the coupling interface, both of which were interpolated through shape function mapping. The schematic diagram of the program is shown in Figure 13.

Cosimulation with MpCCI requires four steps: (1) preparing the model; (2) defining the coupling process; (3) starting cosimulation; (4) postprocessing. First, structure and fluid domains were separately established and discretized, in which coupling regions coupling surfaces were defined and model files were prepared. Simulation codes and versions, coupling surface, coupling algorithm, quantities, coupling step, and coupling time were set in the second step. Next, starting two coupling codes, each code began to calculate its problems, while MpCCI was responsible for controlling the quantities. Finally, the results of each simulation code can be processed by postprocessing tools. Cosimulation solution equations and flowchart are shown in Figure 14.

3.7. Simulation Scenarios. The simulation scenarios in this paper were mainly divided into two parts: (i) the influence of a single physical field on the pipes, i.e., traffic load, pipe fluid, and groundwater, and the influences of the multiphysical fields on the pipes, i.e., combinations of gravity, traffic load, groundwater, and pipe fluid; (ii) parametric analyses of the influence of a single parameter on the pipes under the premise of coupled multiphysical fields were investigated, including a range of traffic loads (P), vehicle speeds (v), bedding strengths (E_b), backfill strengths (E_c), gasket strengths (E_g), soil cover depths (H), groundwater levels (h_w), and fluid heights (h). Simulation scenarios and range of physical variables are shown in Table 6.

4. Failure Criteria

The failure of concrete materials is mainly caused by tensile stress exceeding its ultimate tensile strength. In the CDP constitutive model, when concrete material exceeds its ultimate tensile stress or tensile damage, cracking strain will be generated. Therefore, there are two ways to judge pipe failure: (i) whether the tensile stress exceeds its ultimate

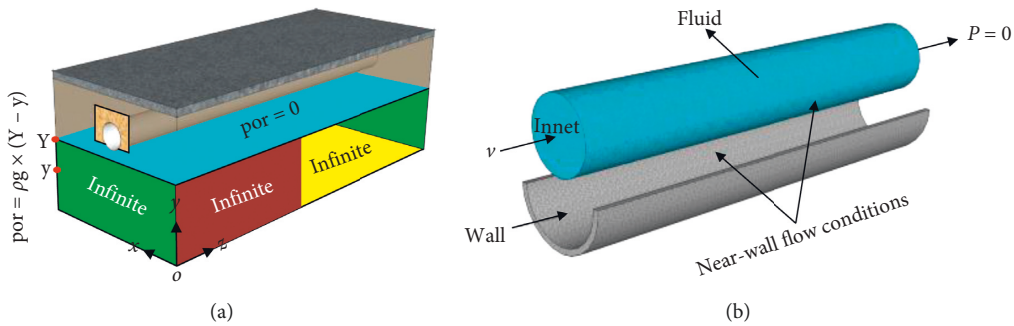

Figure 12: Model boundary conditions for (a) soil-pipe system and (b) pipe wall-fluid.

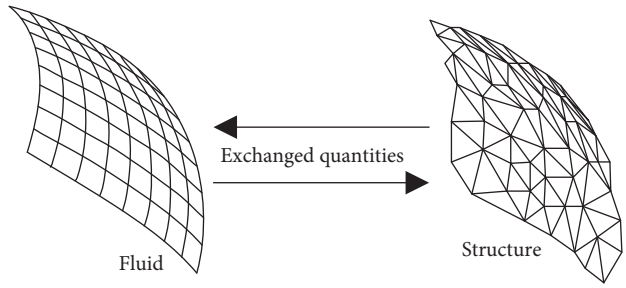

Figure 13: Schematic diagram of the program.

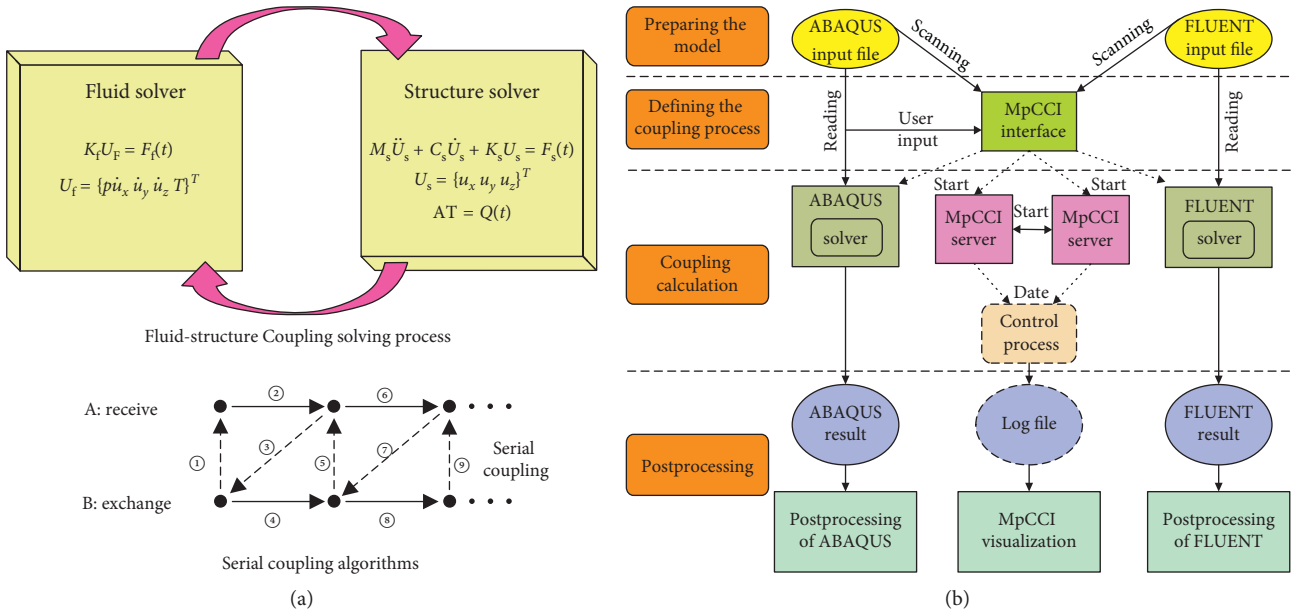

Figure 14: Cosimulation: (a) governing equation and (b) solving flow.

tensile strength and (ii) whether the tensile damage is greater than 1. For C30 concrete pipes used in this study, the tensile yield stress is 2.01 MPa.

5. Results and Discussion

5.1. Validation of FE Model using Field Test. Two groups of vehicle load with different axle loads ($F = 504$ kN and 648 kN, i.e., $P = 0.7$ MPa and 0.9 MPa) moving at a speed of 15 km/s were first used to verify the FE model. In this case, the fluid load was not applied. The maximum hoop principal stresses of the R1-R1 and L1-L1 sections (Figure 2) are plotted in Figure 15.

As shown in Figure 15, under the different vehicle loads, the distributions and amounts of the maximum hoop principal stress of the R1-R1 and L1-L1 sections predicted by

Table 6: Simulation scenarios and range of physical variables.

(*i*)

Physical fields no.	Physical field		Value
Single physical field	Traffic load Pipe fluid Groundwater	+gravity	0.7 MPa 0.25 D 0.5 m above the crown
Multiphysical fields	Gravity, traffic load, groundwater, and pipe fluid		Ibid

(*ii*)

Variable	Range	Variable	Range
Wheel pressure P	0.6–1.5 MPa ($\Delta P = 0.1$)	Gasket strength E_g	2.0–12.0 MPa ($\Delta E_g = 1.0$)
Vehicle speed v	20–90 km/h ($\Delta v = 0.5$)	Soil cover depth H	1.0–3.0 m ($\Delta H = 0.25$)
Bedding strength E_b	100–500 MPa ($\Delta E_b = 50$)	Groundwater level h_w	−1.0–1.0 ($\Delta h_w = 0.25$)
Backfill strength E_c	20.0–100 MPa ($\Delta E_c = 10$)	Fluid height h	0.125–1.0 D ($\Delta h = 0.125$)

Note. A groundwater level of −1.0 m indicates that the groundwater level is 1.0 m below the springline and 1.0 m indicates that the groundwater level is 1.0 m above the springline.

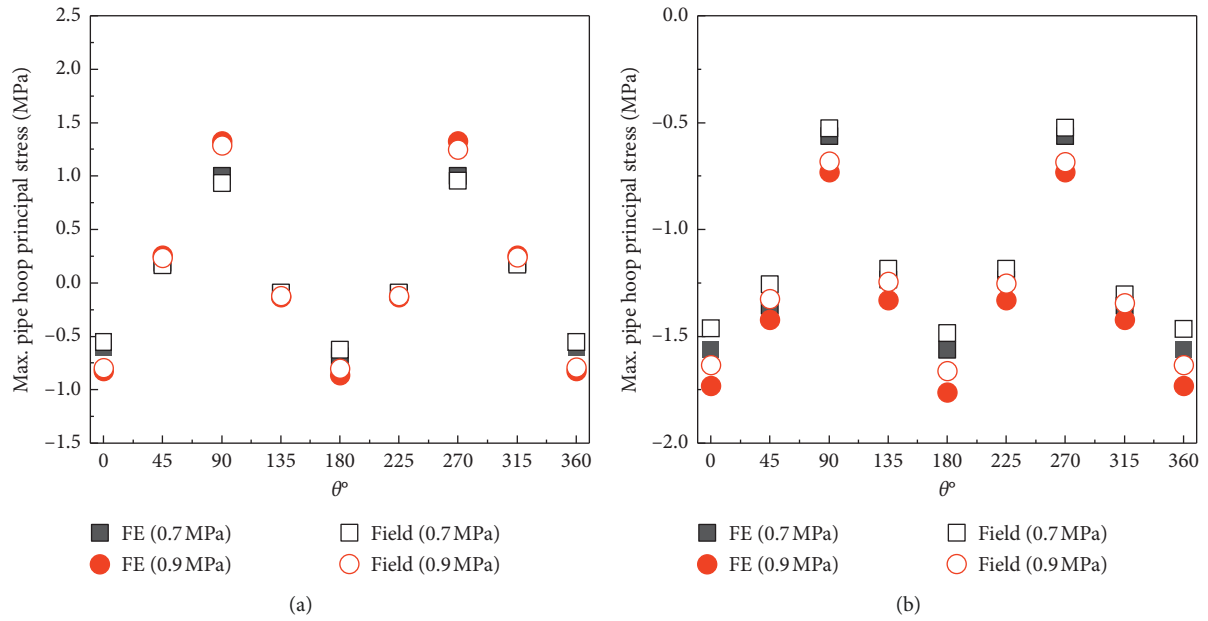

Figure 15: Comparison of hoop principal stress between the FE pipe model and field-instrumented pipe under different vehicle loads. (a) Section R1-R1 and (b) section L1-L1.

the FE model were similar to the data observed by the strain gauges. The largest differences of the maximum hoop principal stresses of the R1-R1 and L1-L1 sections between the FE model and field test were less than 10% and 8%, respectively, indicating that the developed FE model can reliably evaluate the results of the field pipes.

Analyses were also conducted to validate the reliability of the FE model based on two groups field test with fluid heights of 0.25 D and 0.50 D, respectively. In this case, the vehicle load was not applied. The maximum hoop principal stresses of the R1-R1 and L1-L1 sections are shown in Figure 16. It can be seen that the maximum hoop principal stresses between the FE model and field test also show similar distributions and amounts. The maximum differences of the maximum hoop principal stresses of the R1-R1 and L1-L1 sections between the FE model and field test were less than 7% and 5%, respectively, reflecting reliable FE model predictions.

By comparing the maximum hoop principal stresses of the FE model and field test under two groups of vehicle loads with different sizes and fluid loads with different heights, it can be seen that the 3D FE model developed in this study can reliably predict and evaluate the mechanical performances of the pipes, thus ensuring the reliability of the mechanical properties of the pipes under a single physical field and coupled multiphysical fields, as well as the reliability of the parametric analysis results under the premise of coupled multiphysical fields.

5.2. Mechanical Responses of the Drainage Pipe in Single Physical Field and Coupled Multiphysical Fields. Mechanical responses of the concrete pipes in a single physical field and coupled multiphysical fields were investigated based on the validated FE model in this section. The simulation scenarios and physical parameters are shown

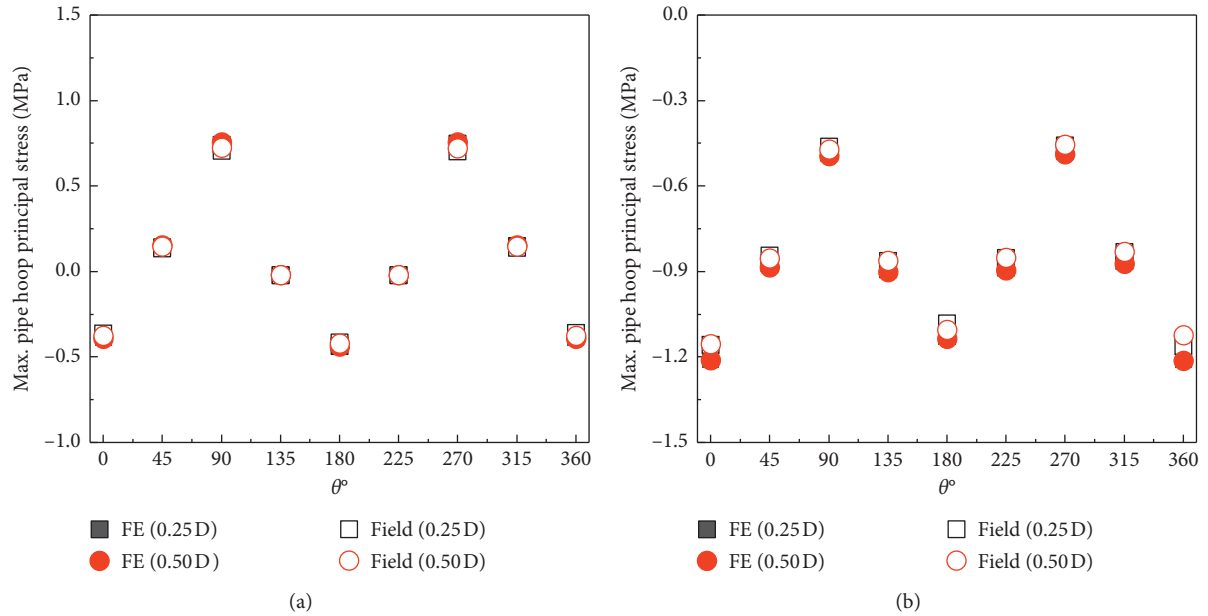

Figure 16: Comparison of hoop principal stress between the FE pipe model and field-instrumented pipe under different fluid heights. (a) Section R1-R1 and (b) section L1-L1.

in Table 5. The maximum hoop principal stress and displacement colormap of the drainage pipe under the conditions of a single physical field and coupled multiphysical fields are shown in Figure 17. The hoop paths of the bell of pipe segment 3 and the spigot and barrel of pipe segment 4 are shown in Figure 17, and the maximum hoop principal stress and radial displacement are plotted in Figures 18 and 19, respectively.

It can be seen from Figure 18(a) that when there is no groundwater (traffic load and fluid act separately), the bell is in compression within 75° from the crown (0–37.5°, 322.5–360°) and within 90° from the invert (135–225°), but in tension in the remaining area. When there is groundwater, the entire bell is in tension. Under the condition of coupled multiphysical fields, the bell is in compression within 45° from the crown (0–22.5°, 337.5–360°) and within 60° from the invert (150–210°), but in tension in the remaining area. Figure 18(b) shows that the spigot is in compression regardless of the presence of groundwater. This is because the gasket has a hoop-binding effect on the spigot, and the gasket expansion force, due to compression, produces a large radial (inward) pressure to the spigot. Figure 18(c) shows that no matter whether there is groundwater or not, the barrel is in compression within 90° from the crown (0–45°, 315–360°) and within 90° from the invert (135–225°), but in tension in the remaining area. The tensile strength of concrete is approximately 0.05 to 0.1 of its compressive strength. Therefore, tensile stress is an indicator of strength control for a concrete pipe. From this perspective, the` spigot is in a good loading condition, but the bell and the springline are most susceptible to tensile damage.

As shown in Figure 19, the radial displacements of the bell, spigot, and barrel are negative in the ranges of 0–90° and 27°–360° and positive in the range of 90–270° (the radial displacement is negative in the direction pointing towards the pipe center). The radial displacement reaches its maximum at the crown and invert and its minimum at the springline, and it is symmetrically distributed about the 0° and 180° axes. In addition, the radial displacement is the largest at the bell, followed by the barrel, and then the spigot.

Based on Figures 18 and 19, the maximum hoop principal stress and radial displacement of the pipe are the largest in the case of the traffic load only, followed by the cases of pipe fluid, coupling, and finally the case of groundwater. The pipe is buried in dry soil in the first two cases, whereas the pipe is buried in saturated soil in the latter two cases, indicating that the forces and deformations of the pipe buried in saturated soil are significantly different from those of the pipe buried in dry soil. Comparisons of the maximum hoop principal stress and radial displacement of the bell, spigot, and barrel under various loading conditions show that the tensile stress is the largest at the springline of the bell, and the radial displacement is the largest at the crown and invert. Effects of groundwater on the maximum hoop principal stress and radial displacement are shown in Table 7.

It can be seen from Table 7 that the tensile stress at the springline and the radial displacement of the crown (invert) under the action of groundwater alone have the greatest reductions compared with the traffic load alone, which are 50.5% and 38.1%, respectively. Randeniya et al. [13] pointed out that when a pipe is buried in nondry soil, the stress is reduced by 10–80% compared to that of dry soil. They suggest this is because in unsaturated soil, the increased stiffness caused by matrix suction resists the pipe movement and deformation. For the numerical results in this paper, the following explanations are given:

(1) For pipes buried in saturated soil, the pore water pressure induced by saturated soil around pipe weakens the local bending and shear displacement

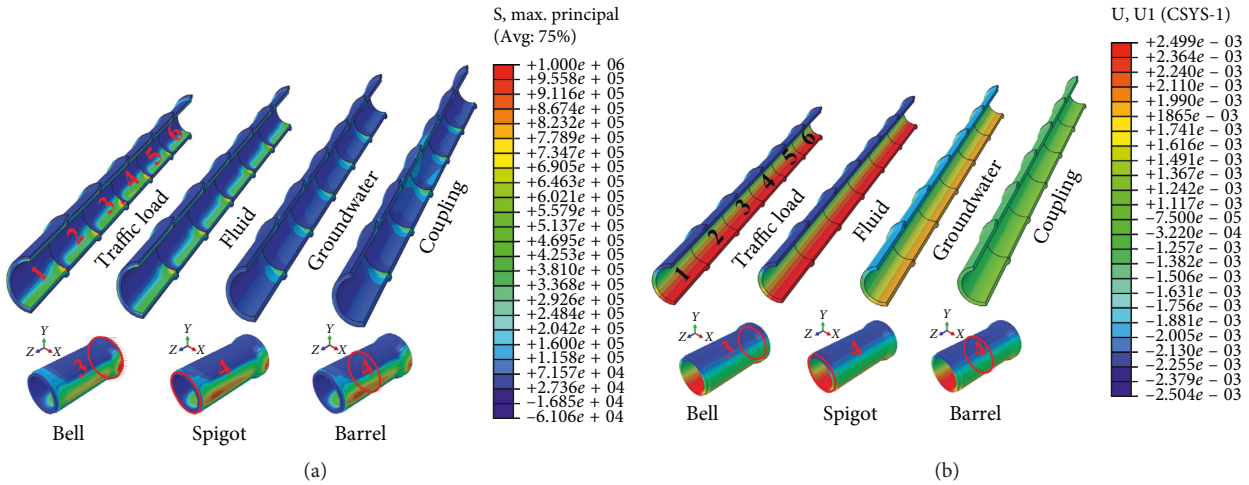

Figure 17: (a) The maximum principal stress and (b) radial displacement of the pipe under the conditions of a single physical field and coupled multiphysical fields.

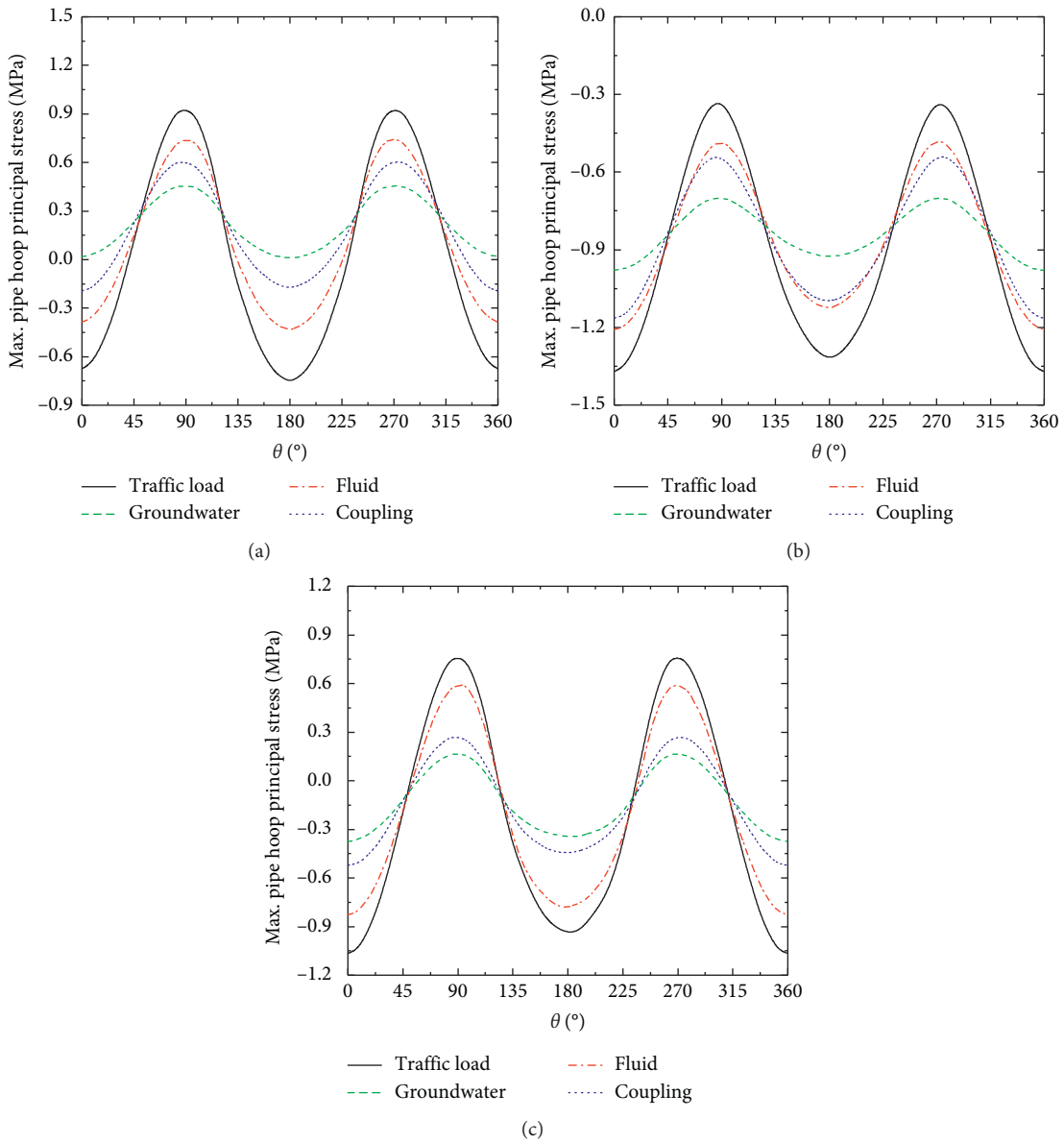

Figure 18: The maximum hoop principal stress under a single physical field and coupled multiphysical fields for (a) bell, (b) spigot, and (c) barrel.

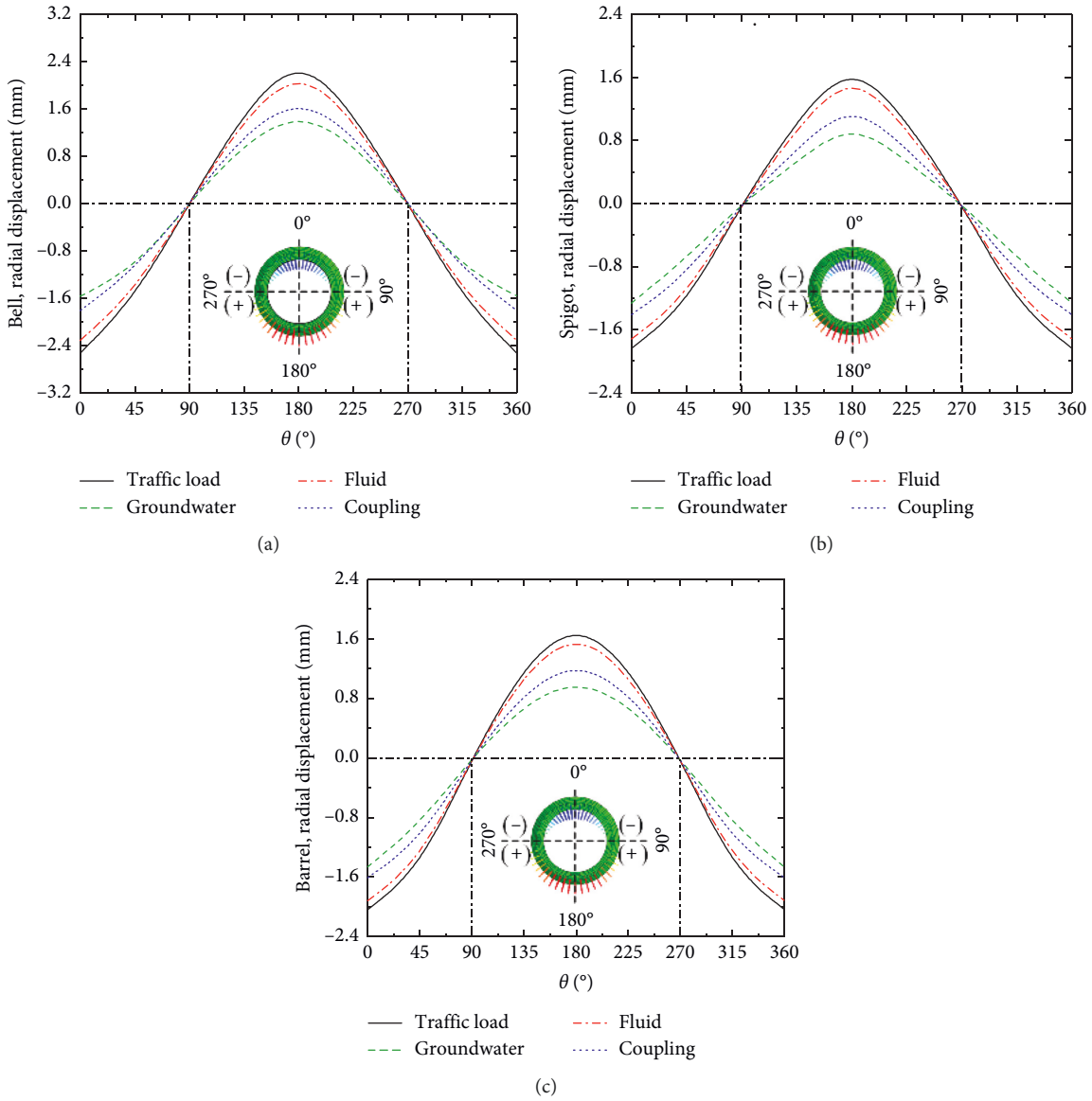

Figure 19: Radial displacement under a single physical field and coupled multiphysical fields for (a) bell, (b) spigot, and (c) barrel.

Table 7: Effect of groundwater on the tensile stress at the springline of the bell and the radial displacement of the crown (invert).

	Traffic load		Pipe fluid		Coupled		Groundwater	
	Stress (MPa)	Displacement (mm)	Stress (MPa)	Displacement (mm)	Stress (MPa)	Displacement (mm)	Stress (MPa)	Displacement (mm)
Value	0.93	2.54	0.74	2.32	0.60	1.81	0.46	1.57
Δ↓ (%)	50.5	38.1	37.8	32.3	30.4	13.2	—	—

caused by traffic loads, thereby reducing both stress and vertical settlement.

(2) The concrete pipe was treated as a material with very low permeability (Table 5). When the pipe is below the groundwater level, the pipe absorbs water from the saturated soil around the pipe while the saturated soil around the pipe dewaters, which promotes the dissipation of pore pressure in the saturated soil around the pipe and thus increases the effective stress, thereby enhancing the constraint on the pipe.

5.3. Parametric Analysis. In Section 5.2, the maximum principal stress of the bell, spigot, and barrel of the drainage pipe under the conditions of a single physical field and coupled multiphysical fields are presented. However, effects

of individual factors on the pipe's mechanical response under the condition of coupled multiphysical fields are unclear. Therefore, under the premise of multifield coupling, the variable controlling method was used to evaluate the effects of the individual factors one by one. Basic parameters are as follows: wheel pressure = 0.7 MPa, vehicle speed = 30 km/h, soil cover depth = 1.0 m, groundwater level is 1.0 m below the springline, bedding strength = 200 MPa, fluid height = 0.25 D, gasket strength = 4 MPa, and backfill strength = 20 MPa, and other physical variables and variation ranges can be seen in Table 6.

5.3.1. Effect of Traffic Load Size. For pipes buried under municipal roads, the traffic load sizes have a direct impact on the mechanical response of the pipes. In order to fully consider different weights (from light to heavy) of municipal vehicles, the wheel pressure in this section was chosen as $P = 0.6–1.5$ MPa ($\Delta P = 0.1$ MPa), and the other parameters are the basic parameters mentioned in Section 5.3. The maximum principal stress and vertical displacement of the pipe under different wheel pressures were extracted and are plotted in Figure 20.

Figure 20 shows that the maximum principal stress and vertical displacement of the pipe increase nearly linearly with the increase in the wheel pressure. When the wheel pressure is 1.5 MPa, the maximum principal stress and vertical displacement increased by 36.7% and 95.8%, respectively, compared with the wheel pressure of 0.6 MPa. Additionally, the maximum principal stress value for a wheel pressure of 1.5 MPa is 2.05 MPa, which is close to the ultimate tensile strength of concrete pipes. According to the full-scale test, the tire grounding shape is a rectangle of 0.2 m × 0.6 m. When the wheel pressure is 1.5 MPa, the axle load of the vehicle is 720 kN. *The Specification for Design of Highway Asphalt Pavement* (JTG D50-2017) [42] stipulates that the standard axle load of a vehicle is 100 kN. When the wheel pressure is 1.5 MPa, the axle load of a vehicle exceeds the specification value by 7.2 times, which is significantly overweight. Rakitin and Xu [5] revealed a similar conclusion that even for a soil cover depth of 4.0 m, heavy traffic load has an obvious effect on pipes. Therefore, the management of overweight vehicles on municipal roads is not only related to the service life and maintenance costs of urban roads but also to the safe operation of municipal pipes buried under the roads.

5.3.2. Effect of Vehicle Speed. As another important parameter of traffic load, the influence of vehicle speed on the mechanical properties of a pipe cannot be ignored. Different vehicle speeds result in different loading times of the traffic loads applied above the pipe, which in turn characterize the difference in the transmission effect of traffic load on soil particles. Because the traffic conditions of municipal roads are complicated and the maximum speed is generally less than 90 km/h, the speed in this section was chosen as $v = 20–90$ km/h ($\Delta v = 5$ km/h), and the other parameters remain the same (i.e., basic parameters). The maximum principal stress and vertical displacement of the pipe at different vehicle speeds are shown in Figure 21.

It can be seen from Figure 21(a) that there is no significant change in the maximum principal stress of the pipe when the vehicle speed is in the range of 20–45 km/h. When the vehicle speed is in the range of 45–75 km/h, there is a significant upward trend, but the increase is less than 1.5%, while there is a gentle downward trend in the range of 75–90 km/h. As can be seen from Figure 7, with the increase in vehicle speed, the variation range of traffic load also increases and becomes more and more obvious. However, when the vehicle speed is in the range of 20–45 km/h, traffic load changes caused by vehicle speed lead to a negligible change in pipe stress. When the vehicle speed is in the range of 45–75 km/h, the traffic load changes caused by vehicle speed result in a slight change in pipe stress. However, when the vehicle speed exceeds 75 km/h, the higher frequency results in a weaker transmission effect of traffic load on soil particles. Figure 21(b) shows that the vertical displacement decreases as the increasing vehicle speed. It indicates that the responses of pipe stress and vertical displacement to vehicle speed are different. Zhang and Shao [12] revealed a similar conclusion that the faster the vehicle speed, the smaller the vertical displacement of the pipe.

The above results show that the curve of maximum principal stress of the buried pipe vs. vehicle speed has two critical values: 45 km/h and 75 km/h. At these two critical values, the trend of the influence of vehicle speed on the maximum principal stress of the pipe changes. The maximum principal stress of the pipe reaches the peak value at the speed of 75 km/h. Meesawasd et al. [6] studied the Mises stress of a pipe at vehicle speeds of 20, 40, 60, and 80 m/s (i.e., 72 km/h, 144 km/h, 216 km/h, and 288 km/h). Results of their study showed that when the vehicle speed was 20 m/s (72 km/h), the vehicle speed had the greatest influence on the Mises stress of the pipe, which agrees well with the results of this study, thus verifying the rationality of the proposed numerical solution method of multiphysical field in this study.

5.3.3. Effect of Bedding Strength. As the supporting structure of the pipe, the reasonable selection of bedding materials is an important measure to prevent uneven settlement, voiding, and other hazards. Bedding materials, which have a particle diameter of less than 25 mm, generally adopt naturally graded sandstone, medium coarse sand, graded gravel, and stone chips. Different materials result in different strengths. In order to fully consider the strengths of different bedding materials, the bedding strength in this section was chosen as $E_b = 100–500$ MPa ($\Delta E_b = 50$ MPa), and the other parameters are kept the same (i.e., basic parameters). The maximum principal stress and the vertical displacement of the pipe under different bedding strengths are shown in Figure 22.

As shown in Figure 22, the maximum principal stress of the pipe increases slowly in the bedding strength range of 100–200 MPa, significantly in the range of 200–400 MPa, and slowly in the range of 400–500 MPa. However, the

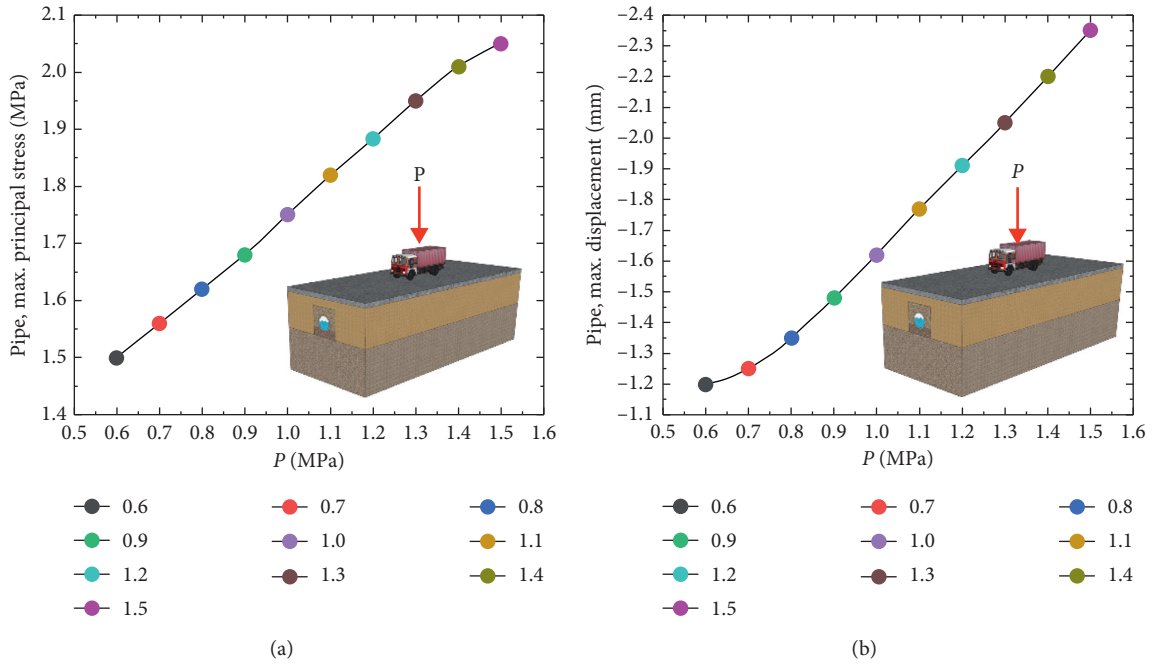

Figure 20: (a) Pipe maximum principal stress vs. wheel pressure. (b) Pipe vertical displacement vs. wheel pressure.

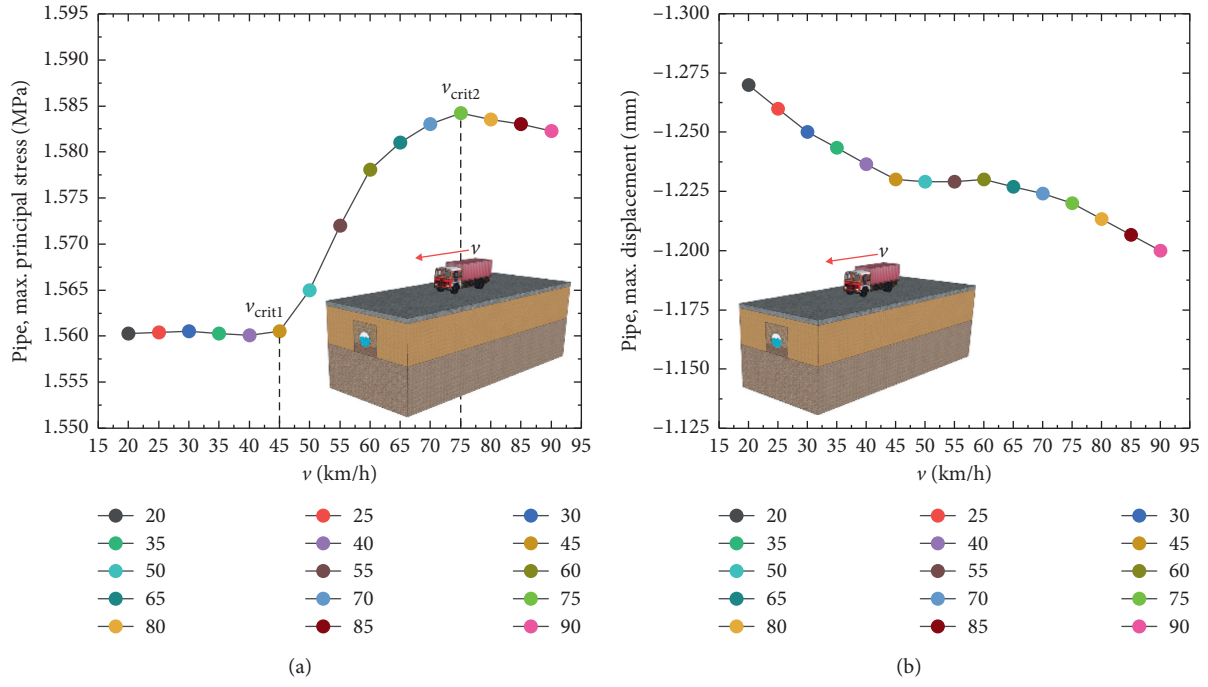

Figure 21: (a) Pipe maximum principal stress vs. vehicle speed. (b) Pipe vertical displacement vs. vehicle speed.

variation of vertical displacement of pipe with bedding strength is contrary to that of maximum principal stress of the pipe. When the bedding strength increases from 100 MPa to 500 MPa, the maximum principal stress and vertical displacement of the pipe increased and decreased by 18.2% and 11.4%, respectively. The results show that increasing the bedding strength enhances the pipe-soil interaction and increases the pressure transmitted to the pipe. Furthermore, it also enhances the constraint on the pipe and thus reduces the vertical settlement of the pipe. Kim et al. [43] evaluated the performance of the plastic foundation for sewage pipes, and the results revealed that the bedding with a lower strength has a tendency to somewhat reduce the load relative to the bedding with a high strength. This conclusion is consistent with the fact revealed in this section.

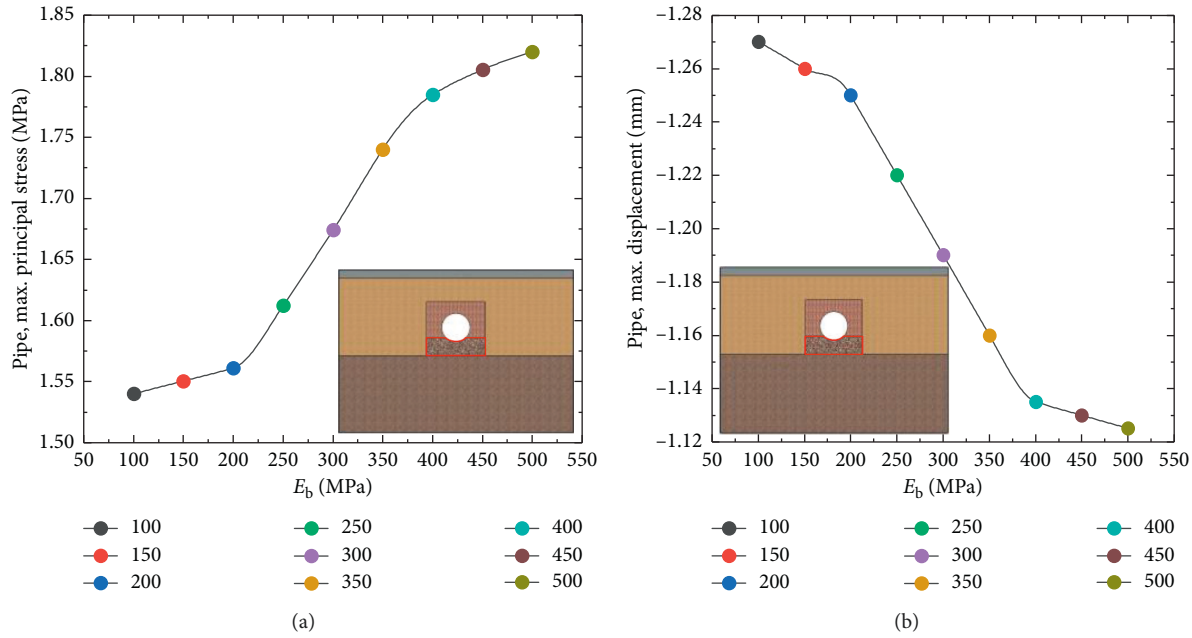

Figure 22: (a) Pipe maximum principal stress vs. bedding strength. (b) Pipe vertical displacement vs. bedding strength.

5.3.4. Effect of Backfill Strength. The *Code for Construction and Acceptance of Water and Sewerage Pipe Works* (GB 50268-2008) [44] has detailed requirements and regulations for backfill between the invert and 500 mm above the crown. The backfill strength varies greatly with the type of backfill, the moisture content, the compacting tools, and the degree of compaction. In this section, the backfill strength was chosen as $E_c = 20$–100 MPa ($\Delta E_c = 10$ MPa), and the other parameters are the basic parameters. Figure 23 shows the maximum principal stress and the vertical displacement of the pipe under different backfill strengths.

As shown in Figure 23, the maximum principal stress of the pipe decreases linearly with the increase in the backfill strength, and the vertical displacement decreases slowly and then rapidly with increasing backfill strength. Furthermore, when the backfill strength increases from 20 MPa to 100 MPa, the maximum principal stress and vertical displacement of the pipe decrease by 20.0% and 10.4%, respectively. This is because an increase in backfill strength enhances the resistance of the pipe to the load above the crown and constrains pipe deformation, which significantly reduces the stress and deformation of the pipe.

5.3.5. Effect of Gasket Strength. A gasket, which is the sealing material of a flexible bell-and-spigot joint, is an important component that ensures no water leakage occurs in the bell-and-spigot joint. The quality of the gasket directly determines the stability of the long-term service performance of the pipe. The Chinese code for *Rubber Seals-joint Rings for Water Supply Drainage and Sewerage Pipe: Specification for Material* (GB/T 21873-2008) [45] has detailed requirements for the performance of gaskets used in water supply and sewage pipes. However, the strength of gaskets varies with the type of gaskets. The gasket strength used in this section is $E_g = 2.0$–12 MPa ($\Delta E_g = 1.0$ MPa), and the other parameters remain the same (i.e., basic parameters). The maximum principal stress and vertical displacement of the pipe under different gasket strengths are shown in Figure 24.

Figure 24(a) shows that the maximum principal stress increases gradually in the range of 2.0–6.0 MPa and abruptly in the range of 6.0–12 MPa. At a gasket strength of 12 MPa, the maximum principal stress reaches a peak value of 2.0 MPa, at which point the pipe is adversely affected. Figure 24(b) shows that with increasing gasket strength, the pipe vertical displacement increases slowly from 2.0 to 5.0 MPa, rapidly from 5.0 to 7.0 MPa, and slowly from 7.0 to 12 MPa. The maximum principal and vertical displacements of the pipe increased by 28.5% and 87.7%, respectively, when the gasket strength increases from 2.0 MPa to 12 MPa.

From the perspective of pipe maximum principal stress, the optimum gasket strength is 6.0 MPa, whereas from the perspective of pipe vertical displacement, the optimum gasket strength is 5.0 MPa. Therefore, it is recommended that the optimum gasket strength be 6.0 MPa for the model presented in this paper.

However, when a gasket material is selected in actual engineering projects, other factors, such as sealing, corrosion resistance, and antiaging, should be considered. It should be noted that García and Moore [3] and Xu et al. [9] concluded that a gasket strength between 1 and 10 MPa does not affect the pipe properties, which is inconsistent with the findings in this study. This discrepancy may be because their studies did not simulate the hoop pressure of the bell-and-spigot joint resulting from compression of the gasket during installation.

5.3.6. Effect of Soil Cover Depth. For municipal pipes, a shallow-buried pipe is generally defined as a pipe with a burial depth of less than 1.5 m and a deep-buried pipe is

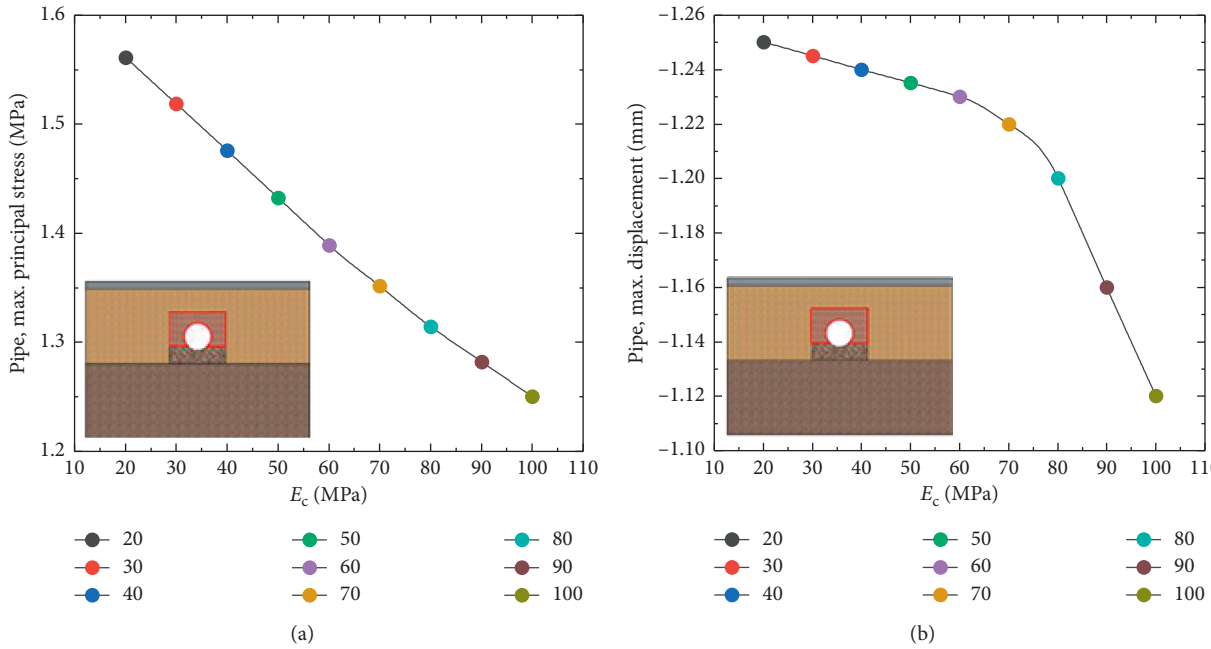

Figure 23: (a) Pipe maximum principal stress vs. backfill strength. (b) Pipe vertical displacement vs. backfill strength.

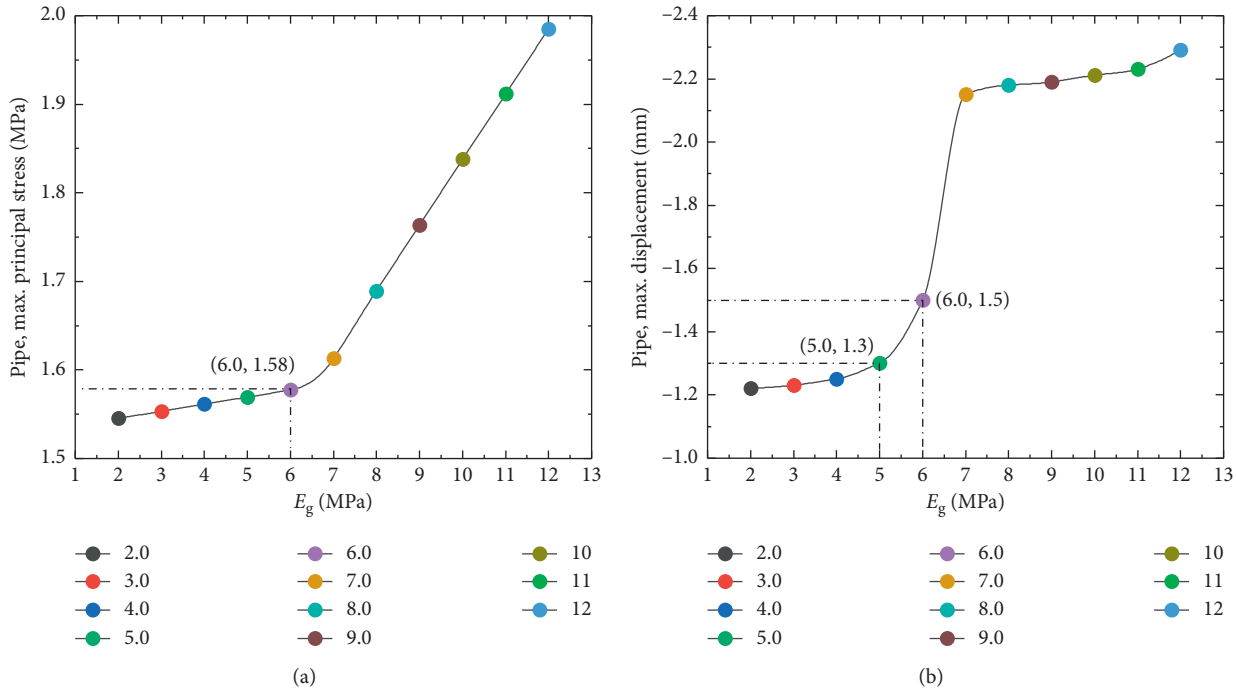

Figure 24: (a) Pipe maximum principal stress vs. gasket strength. (b) Pipe vertical displacement vs. gasket strength.

defined as a pipe with a burial depth of more than 1.5 m. In order to consider the above two types of pipes with different buried depths, the soil cover depth in this section was chosen as $H = 1.0$–3.0 m ($\Delta H = 0.25$ m). The maximum principal stress and the vertical displacement of the pipe under different soil cover depths are shown in Figure 25.

Figure 25(a) shows that the maximum principal stress increases linearly at a high rate from 1.0 to 2.0 m and nonlinearly at a low rate from 2.0 to 3.0 m. Figure 25(b) shows a positive linear correlation between the pipe vertical displacement and the soil cover depth. When the soil cover depth increases from 1.0 m to 3.0 m, the maximum principal stress and vertical displacement of the pipe increased by 34.4% and 124%, respectively. It indicates that the soil cover depth has a great impact on pipe's stress and vertical displacement. In-depth analyses of the influences of the traffic

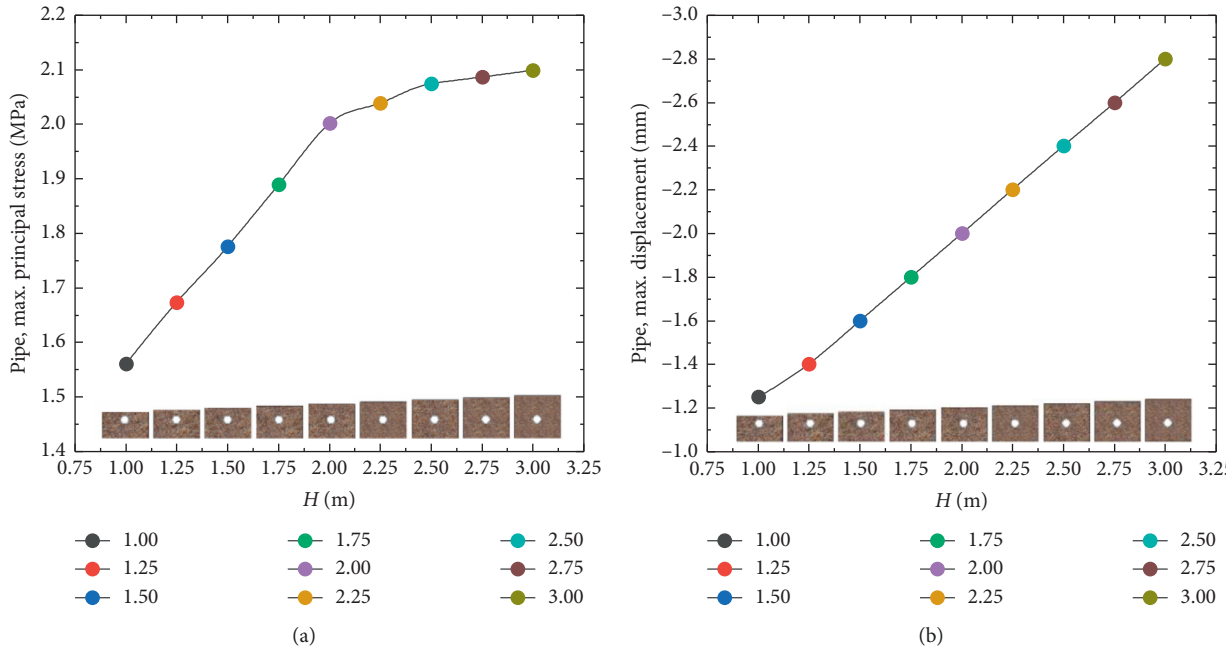

Figure 25: (a) Pipe maximum principal stress vs. soil cover depth. (b) Pipe vertical displacement vs. soil cover depth.

load and the soil cover depth on the pipe stress show that when the soil cover depth is shallow, the pipe is less affected by the earth pressure, and the dissipation effect of the soil on the traffic load is weak. As a result, the pressure transmitted by the traffic load to the pipe is large; thus, the traffic load plays a major role at this time. With increasing soil cover depth, the effect of the traffic load decreases, but the earth pressure increases, and the dissipative effect of the overlying soil on the traffic load is increased at this time, and therefore, the pressure transmitted from the traffic load to the pipe is reduced. At this time, the earth pressure and the traffic load are in a state of "evenly equal force". As the soil cover depth continues to increase, the earth pressure generated by the overlying soil starts to take a leading role, and the effect of the traffic load on the pipe is very weak. Alzabeebee et al. [7] pointed out that when the soil cover depth reaches 3.0 m, the effect of the traffic load is insignificant. These results are consistent with the findings in this study.

5.3.7. Effect of Groundwater Level. The *Code for Construction and Acceptance of Water and Sewerage Pipe Works* (GB 50268-2008) [44] requires that the groundwater level should be at least 0.5 m below the trench base. If the above requirement is not met, the groundwater level should be lowered. However, it is unavoidable that the buried pipelines in service are submerged by groundwater, especially in areas where the groundwater level is very shallow. Therefore, in order to study the influence of groundwater level on a buried concrete pipe, the groundwater level in this section was chosen as $h_w = -1.0$–1.0 m ($\Delta h_w = 0.25$ m). The maximum principal stress and the vertical displacement of the pipe under different groundwater levels are shown in Figure 26.

Figure 26 shows that the maximum principal stress and vertical displacement of the pipe decrease significantly with increasing groundwater level. At a groundwater level of −0.5 m (i.e., the groundwater level at the invert), rates of the maximum principal stress and vertical displacement abruptly change. When the groundwater level is lower than −0.5 m (i.e., the pipe was all buried in dry soil), the maximum principal stress and vertical displacement decrease very little. By contrast, when the groundwater level is higher than −0.5 m (i.e., the pipe was buried in partially saturated-partially dry soil to fully saturated soil), the maximum principal stress and vertical displacement of the pipe decrease rapidly at a constant rate. Additionally, when the groundwater level rises from −0.5 m to +1.0 m, the maximum principal stress and vertical displacement of the pipe are reduced by 43.2% and 46.6%, respectively.

The mechanism of pipe loading due to groundwater can be explained as follows: when the groundwater level is from −1.0 m to −0.5 m (i.e., the groundwater level is lower than the invert), the pipe was buried in dry soil. Therefore, the stress and vertical displacement of the pipe decrease slowly. When the groundwater level is above −0.5 m, part or all of the pipe is surrounded by saturated soil, causing the pipe to absorb water from the saturated soil. As a result, the pore pressure of the saturated soil around the pipe dissipates, and the effective stress increases. Hence, the restraint to the pipe is increased. At the same time, the pore water pressure induced by the saturated soil around the pipe weakens the local bending stress and vertical settlement caused by the traffic load. Therefore, the maximum principal stress and vertical displacement of the pipe are drastically reduced.

Randeniya et al. [13] investigated the effect of traffic loads on the stress distribution of a pipe buried in unsaturated soil based on a 2D FE model. The results showed

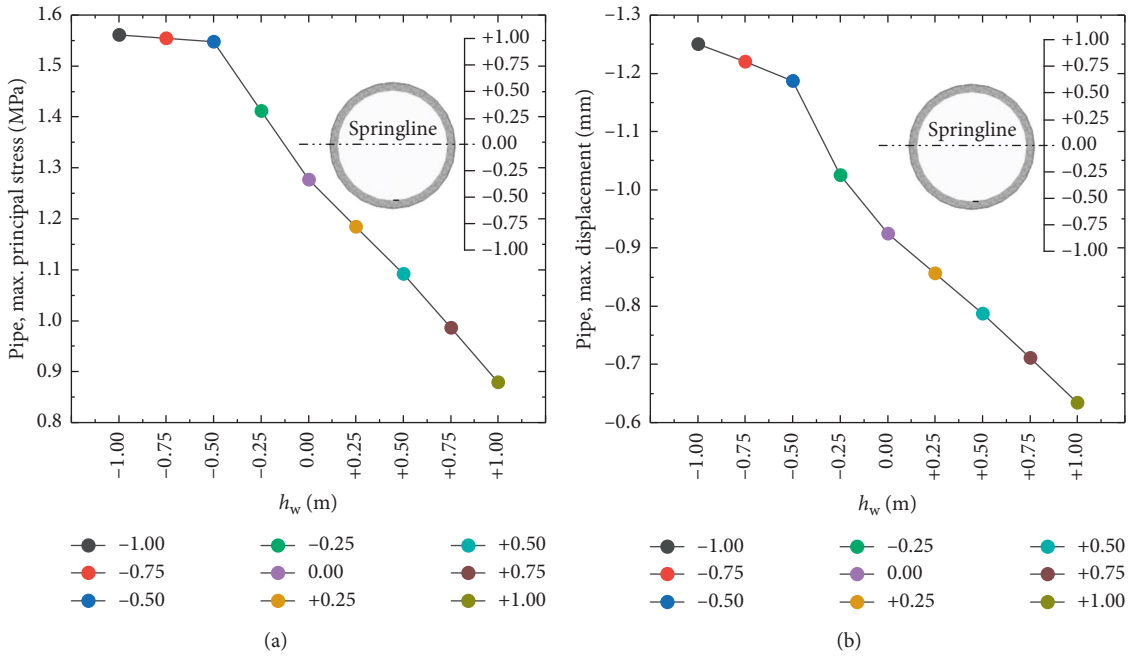

Figure 26: (a) Pipe maximum principal stress vs. groundwater level. (b) Pipe vertical displacement vs. groundwater level.

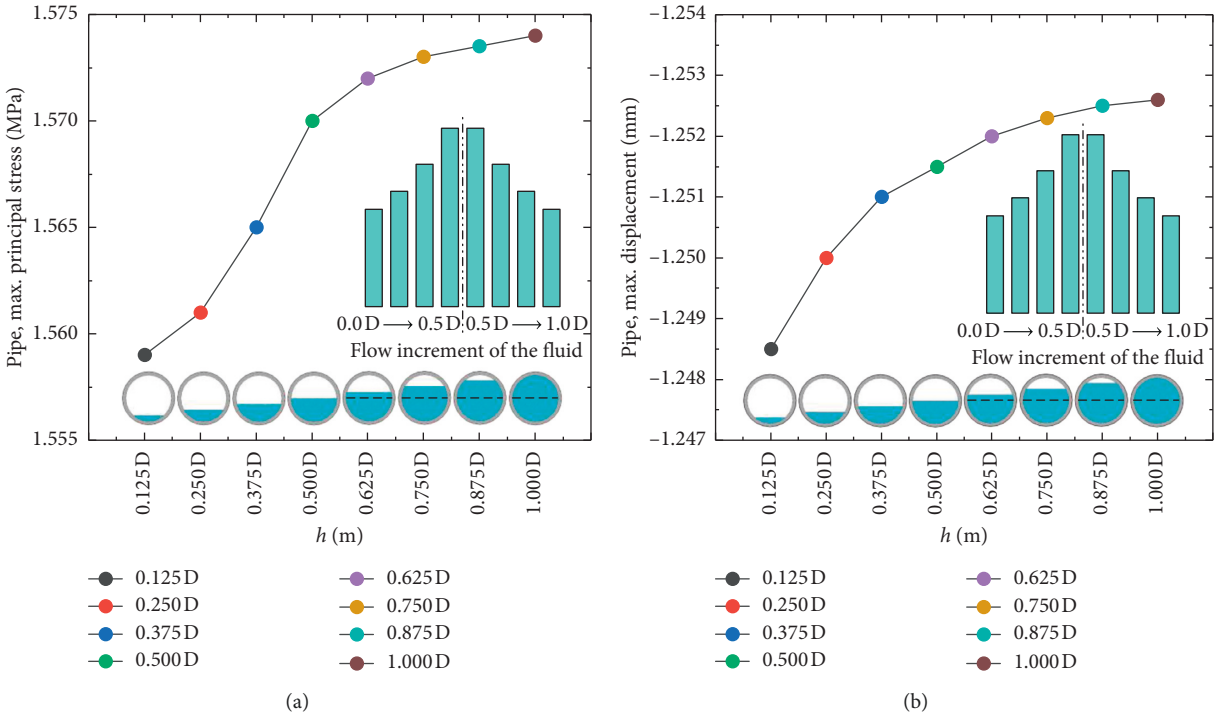

Figure 27: (a) Pipe maximum principal stress vs. pipe fluid height. (b) Pipe vertical displacement vs. pipe fluid height.

that the pipe hoop stresses were lowered by 10%–80% when the pipeline was buried in nondry soil (soil saturation is 20% and 60%) when compared to the response in dry soil. The buried condition of the pipeline in this study is more complicated than that in the study by Randeniya et al. [13] (as the groundwater level rises, the pipe buried conditions were dry, unsaturated, and saturated). However, the variation trends of stress and vertical displacement of the pipe are similar to the conclusions in [13].

5.3.8. Effect of Pipe Fluid Height. The drainage volume of concrete drainage pipes varies greatly with time due to factors such as high and low peak periods of domestic water

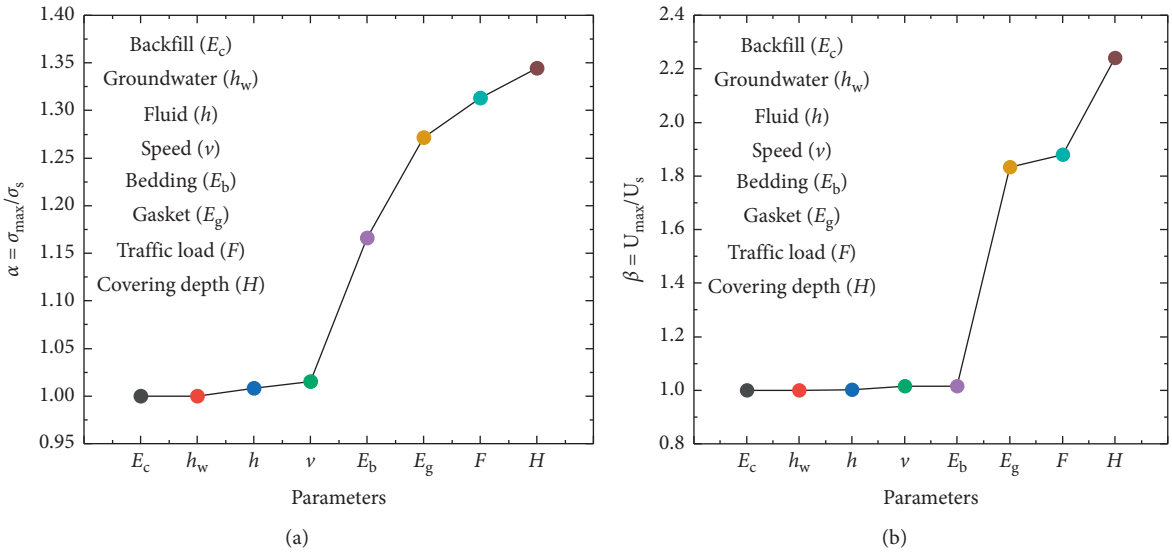

Figure 28: Normalization of the (a) maximum principal stress and (b) vertical displacement.

and rainfall. In this section, the flow in the pipe is defined as the ratio of the fluid height to the inner diameter of the pipe. In order to simulate the flow rates of a drainage pipe at different flow levels, a value of $h = 0.125\,\mathrm{D}$–$1.0\,\mathrm{D}$ ($\Delta h = 0.125\,\mathrm{D}$) was chosen. The maximum principal stress and the vertical displacement of the pipe at different fluid heights are shown in Figure 27.

The maximum principal stress and vertical displacement of the pipe are positively correlated with the fluid height. However, the overall effect is not obvious. Figure 28 shows that when the fluid height is less than 0.5 D, the rates of increase of the maximum principal stress and vertical displacement are larger than when the fluid height is greater than 0.5 D. The analysis concludes that this is because the fluid volume increment gradually increases when the fluid height increases in the pipe from 0.0 D to 0.5 D, whereas the fluid volume increment gradually decreases when the fluid height increases from 0.5 D to 1.0 D.

5.4. Sensitivity Analysis. In Section 5.3, the influence mechanisms of each individual factor on the mechanical response of the pipe were identified. However, it is still unclear which factor the pipe response is most sensitive to. In this section, the maximum principal stress (σ_{max}) and vertical displacement (U_{max}) for each set of parameters are normalized by the maximum principal stress (σ_s) and vertical displacement (U_s) calculated from the basic parameters, and the results are plotted in Figure 28.

As shown in Figure 28, the parameters that have a relatively large influence on the maximum principal stress and vertical displacement of the pipe are soil cover depth, traffic load size, and gasket strength. The bedding strength has a large influence on the maximum principal stress but little influence on the vertical displacement. We note that the maximum principal stress and vertical displacement corresponding to the groundwater level were obtained based on the basic parameters, resulting in a normalization coefficient of 1 as shown in Figure 28. However, it is known from previous sections that the groundwater level has a large influence (negatively correlated) on the maximum principal stress and vertical displacement.

6. Conclusions

This paper focuses on the problem that the mechanical behavior of a concrete drainage pipe is not clear under coupled multiphysical field, combined with the on-site full-scale test and numerical methods, the mechanical properties of the drainage pipe coupled multiphysical field are studied, and the following main conclusions are obtained:

(1) The proposed new numerical solution method for coupled stress, seepage, and flow fields could accurately predict the pipe stress distributions and amounts observed by the strain gauges, indicating that this method could be used to evaluate the mechanical behaviors of the concrete drainage pipes under coupled multiphysical field.

(2) Under the conditions of a single physical field and coupled multiphysical fields, the maximum hoop principal stress and radial displacement of the pipe are the largest in the case of traffic load only. This is followed by cases including pipe fluid, coupled multiphysical fields, and groundwater, indicating that the stress and displacement of a pipe buried in saturated soil are different from those of a pipe buried in dry soil. Under the action of groundwater alone, the tensile stress at the springline and the radial displacement of the crown (invert) of the bell are reduced by 50.5% and 38.1%, respectively, compared to the traffic load alone.

(3) Parametric analyses show that the maximum principal stress and vertical displacement of the pipe are

linearly and positively correlated with traffic load, indicating that an overweight vehicle has a large influence on the stress and deformation of a buried pipe. An increase in the bedding strength enhances the pipe-soil interaction and therefore increases the pressure transmitted to the pipe; however, at the same time, this process constrains the vertical displacement of the pipe. Therefore, it is important to consider both pipe stress and settlement when selecting a reasonable bedding strength. The maximum principal stress and vertical displacement of the pipe are negatively correlated with backfill strength, indicating that an increase in backfill strength can enhance the resistance to the load above the pipe. The gasket strength is positively correlated with the maximum principal stress and vertical displacement of the pipe. For the model built in this study, the optimum gasket strength is 6.0 MPa. The maximum principal stress and vertical displacement of the pipe increase with increasing soil cover depth. After the soil cover depth reaches 2.0 m, the influence of a traffic load on the pipe begins to decrease. When the soil cover depth reaches 3.0 m, the traffic load has no obvious influence on the pipe. The maximum principal stress and vertical displacement rapidly decrease with increasing groundwater level. However, the results show that the effects of vehicle speed and fluid height on the pipe are not significant.

(4) Sensitivity analysis shows that soil cover depth has the greatest influence on the maximum principal stress and vertical displacement of the pipe, followed by the traffic load and backfill strength.

Abbreviations

f: Frequency of excitation
C_s: Shear-wave velocity
Δl: Maximum mesh element size
ω: Circular frequency of excitation
C_u: 0.0845
$C_{\varepsilon 1}$: 1.42
$C_{\varepsilon 2}$: 1.68
η_0: 4.377
β: 0.012
F_t: Dynamic vehicle wheel load
F: Static vehicle wheel load
G_0: Unsprung weight
$\mu_{\omega/r}(y)$: Mroad roughness function
k: Permeability coefficient
v: Vehicle speed
t: Moving time of traffic load
E: Elastic modulus
ν: Poisson's ration
ρ: Density
φ: Friction angle
α: Damping
σ_{max}: Maximum pipe stress
l: Geometric curve wavelength of the pavement
e: Void ratio
ψ: Dilation angle
μ: Viscosity parameter of concrete pipe
f_1, f_2: Attenuation functions
ξ: Natural coordinate
N_i': Shape function at the node of finite element
η_i: Value of η at node i
ζ_i: Value of ζ at node i
r: Radial distance
r_1, r_2: Distance of nodes 1 and 2 of the infinite element in the physical plane
Y: Coordinate value of the groundwater level
y: Coordinate value of any point below the groundwater level
por: Pore water pressure
U_p: Average flow rate of the fluid at point P
k_p: Turbulent kinetic energy at point P
y_p: Distance from point P to the wall
μ^*: Dynamic viscosity coefficient of the fluid
ρ_w: Mass density of water
A: Area of each tire
P: Pressure of each tire applied to the ground
F: Total weight of the truck and rated blocks.

Data Availability

The data used to support the findings of this study are included within the article.

Conflicts of Interest

The authors declare that there are no conflicts of interest regarding the publication of this paper.

Acknowledgments

This research was supported by the National Key Research and Development Program of China (No. 2016YFC0802400), the National Natural Science Foundation of China (No. 51678536), the Scientific and Technological Research Program of Henan Province (No. 152102310066), and the Outstanding Young Talent Research Fund of Zhengzhou University (1621323001), for which the authors are grateful. Special thanks go to Tsinghua University for its support with the MpCCI software.

References

[1] N. S. M. Fernando and J. P. Carter, "Elastic analysis of buried pipes under surface patch loadings," *Journal of Geotechnical and Geoenvironmental Engineering*, vol. 124, no. 8, pp. 720–728, 1998.

[2] M. A. Noor and A. S. Dhar, "Three-dimensional response of buried pipe under vehicle loads," in *Proceedings of the ASCE International Conference on Pipe Engineering and Construction*, vol. 1, pp. 658–665, American Society of Civil Engineers, Baltimore, MD, USA, 2003 July.

[3] D. B. García and I. D. Moore, "Behaviour of bell and spigot joints in buried reinforced concrete pipelines," *Canadian Geotechnical Journal*, vol. 52, no. 5, pp. 609–625, 2015.

[4] G. R. Lay and R. W. I. Brachman, "Full-scale physical testing of a buried reinforced concrete pipe under axle load," *Canadian Geotechnical Journal*, vol. 51, no. 4, pp. 394–408, 2014.

[5] B. Rakitin and M. Xu, "Centrifuge modeling of large-diameter underground pipes subjected to heavy traffic loads," *Canadian Geotechnical Journal*, vol. 51, no. 4, pp. 353–368, 2014.

[6] N. Meesawasd, C. Boonyasiriwat, S. Kongnuan, and F. Chamchod, "Finite element modeling for stress analysis of a buried pipeline under soil and traffic loads," in *Proceedings of the 2016 IEEE International Conference on Industrial Engineering and Engineering Management (IEEM)*, pp. 385–390, Bali, Indonesia, December 2016.

[7] S. Alzabeebee, D. Chapman, I. Jefferson, and A. Faramarzi, "The response of buried pipes to UK standard traffic loading," *Proceedings of the Institution of Civil Engineers-Geotechnical Engineering*, vol. 170, no. 1, pp. 38–50, 2017.

[8] B. Rakitin and M. Xu, "Centrifuge testing to simulate buried reinforced concrete pipe joints subjected to traffic loading," *Canadian Geotechnical Journal*, vol. 52, no. 11, pp. 1762–1774, 2015.

[9] M. Xu, D. Shen, and B. Rakitin, "The longitudinal response of buried large-diameter reinforced concrete pipeline with gasketed bell-and-spigot joints subjected to traffic loading," *Tunnelling and Underground Space Technology*, vol. 64, pp. 117–132, 2017.

[10] Y. Wang, Y. Gao, B. Li et al., "One-way cyclic deformation behavior of natural soft clay under continuous principal stress rotation," *Soils and Foundations*, vol. 57, no. 6, pp. 1002–1013, 2017.

[11] Y. Wang, Y. Gao, B. Li, L. Guo, Y. Cai, and A. H. Mahfouz, "Influence of initial state and intermediate principal stress on undrained behavior of soft clay during pure principal stress rotation," *Acta Geotechnica*, vol. 14, no. 5, pp. 1–23, 2019.

[12] T. Q. Zhang and Y. Shao, "Dynamic analyses of pipes in saturated soil under traffic loads," *Journal of Zhejiang University (Engineering Science)*, vol. 41, no. 1, pp. 48–51, 2007.

[13] C. Randeniya, D. Robert, and C. Li, "The effect of traffic loading to buried water mains in partially saturated soils," in *Proceedings of the 6th Asia Pacific Conference on Unsaturated Soils*, pp. 23–26, Guilin, China, October 2015.

[14] M. Al-Khazaali, S. K. Vanapalli, and W. T. Oh, "Numerical investigation of soil–pipeline system behavior nearby unsupported excavation in saturated and unsaturated glacial till," *Canadian Geotechnical Journal*, vol. 56, no. 1, pp. 69–88, 2019.

[15] D. J. Robert and N. I. Thusyanthan, "Uplift resistance of buried pipelines in partially saturated sands," *Computers and Geotechnics*, vol. 97, pp. 7–19, 2018.

[16] E. S. Williams, B. W. Byrne, and A. Blakeborough, "Pipe uplift in saturated sand: rate and density effects," *Géotechnique*, vol. 63, no. 11, pp. 946–956, 2013.

[17] A. S. Tijsseling, "Fluid-structure interaction in liquid-filled pipe systems: a review," *Journal of Fluids and Structures*, vol. 10, no. 2, pp. 109–146, 1996.

[18] D. C. Wiggert and A. S. Tijsseling, "Fluid transients and fluid-structure interaction in flexible liquid-filled piping," *Applied Mechanics Reviews*, vol. 54, no. 5, pp. 455–481, 2001.

[19] A. M. Belostosky, P. A. Akimov, and T. B. Kaytukov, "About finite element analysis of fluid–structure interaction problems," *Procedia Engineering*, vol. 91, pp. 37–42, 2014.

[20] D. Ferràs, P. A. Manso, A. J. Schleiss, and D. I. C. Covas, "Fluid-structure interaction in straight pipelines: friction coupling mechanisms," *Computers & Structures*, vol. 175, pp. 74–90, 2016.

[21] B. Li, H. Fang, H. He, K. Yang, C. Chen, and F. Wang, "Numerical simulation and full-scale test on dynamic response of corroded concrete pipelines under multi-field coupling," *Construction and Building Materials*, vol. 200, pp. 368–386, 2019.

[22] B. Y. Dagli and A. Ergut, "Dynamics of fluid conveying pipes using Rayleigh theory under non-classical boundary conditions," *European Journal of Mechanics—B/Fluids*, vol. 77, pp. 125–134, 2019.

[23] General Administration of Quality Supervision, Inspection and Quarantine of the People's Republic of China, Standardization Administration of the People's Republic of China, *Concrete and Reinforced Concrete Sewer Pipes (GB/T 11836–2009)*, Standards Press of China, Beijing, China, 2009.

[24] M. Balkaya, I. D. Moore, and A. Sağlamer, "Study of non-uniform bedding due to voids under jointed PVC water distribution pipes," *Geotextiles and Geomembranes*, vol. 34, pp. 39–50, 2012.

[25] J. Buco, F. Emeriault, P. Le Gauffre, and R. Kastner, "Statistical and 3D numerical identification of pipe and bedding characteristics responsible for longitudinal behavior of buried pipe," in *Proceedings of the 2006 Pipe Division Specialty Conference—Pipes 2006: Service to the Owner*, vol. 211, p. 83, July-August 2006.

[26] S. Messioud, U. S. Okyay, B. Sbartai, and D. Dias, "Dynamic response of pile reinforced soils and piled foundations," *Geotechnical and Geological Engineering*, vol. 34, no. 3, pp. 789–805, 2016.

[27] M. Frank, R. Kamenicky, D. Drikakis, L. Thomas, H. Ledin, and T. Wood, "Multiphase flow effects in a horizontal oil and gas separator," *Energies*, vol. 12, no. 11, p. 2116, 2019.

[28] Q. Yuan, C. Wang, Y. Wang, C. Peng, and X. Meng, "Investigation of submerged soil excavation by high-velocity water jet using two-fluid smoothed particle hydrodynamics method," *Journal of Hydraulic Engineering*, vol. 145, no. 6, Article ID 04019016, pp. 1–15, 2019.

[29] T. Treeratanaphitak and N. M. Abukhdeir, "Phase-bounded finite element method for two-fluid incompressible flow systems," *International Journal of Multiphase Flow*, vol. 117, pp. 1–13, 2019.

[30] S. Huang, X. Su, and G. Qiu, "Transient numerical simulation for solid-liquid flow in a centrifugal pump by DEM-CFD coupling," *Engineering Applications of Computational Fluid Mechanics*, vol. 9, no. 1, pp. 411–418, 2015.

[31] S. Ghorai and K. D. P. Nigam, "CFD modeling of flow profiles and interfacial phenomena in two-phase flow in pipes," *Chemical Engineering and Processing: Process Intensification*, vol. 45, no. 1, pp. 55–65, 2006.

[32] Y. G. Lai, L. J. Weber, and V. C. Patel, "Nonhydrostatic three-dimensional model for hydraulic flow simulation. I: formulation and verification," *Journal of Hydraulic Engineering*, vol. 129, no. 3, pp. 196–205, 2003.

[33] Y. Zhuang and S. Li, "Three-dimensional finite element analysis of arching in a piled embankment under traffic loading," *Arabian Journal of Geosciences*, vol. 8, no. 10, pp. 7751–7762, 2015.

[34] J. Lee and G. L. Fenves, "Plastic-damage model for cyclic loading of cement structures," *Journal of Engineering Mechanics*, vol. 124, no. 8, p. 900, 1998.

[35] J. M. Kurdziel, "Design of profile gaskets for corrugated polyethylene pipe," in *Proceedings of the ASCE Pipe Division Specialty Congress—Pipe Engineering and Construction—What's on the Horizon, PIPES 2004*, pp. 889–898, American Society of Civil Engineers, San Diego, CA, USA, August 2004.

[36] D. B. García and I. D. Moore, "Rotational characteristics of a gasketed bell and spigot joint in a pressurized reinforced concrete pipe," *Journal of Pipeline Systems Engineering and Practice*, vol. 7, no. 1, Article ID 04015010, 2016.

[37] P. Vazouras, S. A. Karamanos, and P. Dakoulas, "Mechanical behavior of buried steel pipes crossing active strike-slip faults," *Soil Dynamics and Earthquake Engineering*, vol. 41, pp. 164–180, 2012.

[38] P. Kumar, "Infinite elements for numerical analysis of underground excavations," *Tunnelling and Underground Space Technology*, vol. 15, no. 1, pp. 117–124, 2000.

[39] M. L. Li, "Study on flow pattern of concrete based on PIV and fluent," Master's thesis, Chongqing University, Chongqing, China, 2013.

[40] B. Steckel, *MpCCI–Mesh Based Parallel Code Coupling Interface, GMD, 2nd MpCCI User Forum*, Institute for Algorithms and Scientific Computing (SCAI), Sankt Augustin, Germany, 2000, http://publica.fraunhofer.de/documents/B-73148.html.

[41] W. Joppich and M. Kürschner, "MpCCI—a tool for the simulation of coupled applications," *Concurrency and Computation Practice and Experience*, vol. 18, no. 2, pp. 183–192, 2006.

[42] Ministry of Transport of the People's Republic of China, *Specification for Design of Highway Asphalt Pavement (JTG D50-2017)*, China Communications Press, Beijing, China, 2017.

[43] S. K. Kim, D. H. Lee, and K. H. Lee, "Performance evaluation of a plastic foundation for sewage pipeline," *Journal of Testing and Evaluation*, vol. 44, no. 1, pp. 237–247, 2016.

[44] Ministry of Housing and Urban-Rural Development of the People's Republic of China, General Administration of Quality Supervision, Inspection and Quarantine of the People's Republic of China, *Code for Construction and Acceptance of Water and Sewerage Pipe Works (GB 50268-2008)*, China Architecture & Building Press, Beijing, China, 2008.

[45] General Administration of Quality Supervision, Inspection and Quarantine of the People's Republic of China, Standardization Administration of the People's Republic of China, *Rubber Seals-joint Rings for Water Supply Drainage and Sewerage Pipe-Specification for Material (GB/T 21873-2008)*, Standards Press of China, Beijing, China, 2008.